International Journal of Earth Sciences (2018) 107:1807–1833
https://doi.org/10.1007/s00531-017-1573-7

ORIGINAL PAPER

Gravimetric and magnetic fabric study of the Sintra Igneous complex: laccolith-plug emplacement in the Western Iberian passive margin

Pedro Terrinha[1] · Emilio L. Pueyo[2,3] · Aitor Aranguren[4] · José Carlos Kullberg[5] · Maria Carla Kullberg[6] · Antonio Casas-Sainz[7] · Maria do Rosário Azevedo[8]

Received: 27 March 2017 / Accepted: 8 December 2017 / Published online: 14 December 2017

Abstract
The geometry and emplacement of the ~96 km^2, Late Cretaceous Sintra Igneous complex (SIC, ca. 80 Ma) into the West Iberian passive margin is presented, based on structural data, gravimetric modeling, and magnetic fabrics. A granite laccolith (~76 km^2, <1 km thick, according to gravimetric modeling) surrounds a suite of gabbro–diorite–syenite plugs (~20 km^2, ~4 km deep) and is encircled by cone sheets and radial dykes. Anisotropy of Magnetic Susceptibility was interpreted from 54 sites showing fabrics of para- and ferro-magnetic origin. Most fabrics can be interpreted to have a magmatic origin, according to the scarcity of solid-state deformation in most part of the massif. Magnetic foliations are shallowly dipping in the granite laccolith and contain a sub-horizontal ENE–WSW lineation. The gabbro–syenite body displays concentric magnetic foliations having variable dips and steeply-plunging lineations. The SIC can be interpreted to be intruded along an NNW–SSE, 200 km-long fault, perpendicular to the magnetic lineation within the laccolith, and was preceded by the intrusion of basic sills and plugs. The SIC intruded the Mesozoic series of the Lusitanian Basin during the post-rift, passive margin stage, and its geometry was only slightly modified during the Paleogene inversion that resulted in thrusting of the northern border of the intrusion over the country rocks.

Keywords Sintra · Anisotropy of magnetic susceptibility · Gravimetry · Cretaceous alkaline magmatism · West Iberia margin

Introduction

Magmatic bodies are excellent markers of their tectonic context and evolution because of the possibility of absolute, radiometric dating together with the characterization of the strain field contemporary (magmatic fabric) or post-dating (solid-state or brittle fabrics) intrusions (e.g., Bouchez et al. 1990; Gleizes et al. 1993; Nédelec and Bouchez 2015). In this sense, granite intrusions are especially useful under weak deformation periods or anorogenic settings (see, e.g., Pearce 1996; Aranguren et al. 2003; Calvín et al. 2017, and references therein), when other deformation markers (syn-tectonic sedimentation, metamorphism, etc.) are absent. Magma flow revealed by magmatic fabrics can give in this case information about strain axes and main active faults (Román-Berdiel et al. 1995a; Izquierdo-Llavall et al. 2012).

✉ Antonio Casas-Sainz
acasas@unizar.es

[1] Division of Marine Geology and Georesources, IPMA, IDL, 1749-077 Lisboa, Portugal

[2] Instituto Geológico y Minero de España, Unidad de Geologia y Geofísica, Zaragoza, Spain

[3] Unidad Asociada IGME/Universidad de Zaragoza, Zaragoza, Spain

[4] Departamento de Geodinámica, Facultad de Ciencia y Tecnología, Universidad del País Vasco UPV/EHU, Apdo. 644, 48080 Bilbao, Spain

[5] Centro de Investigação em Ciência e Engenharia Geológica (CICEGe), Universidade Nova de Lisboa, Quinta da Torre, Monte de Caparica, 2829-516 Caparica, Portugal

[6] Departamento de Geologia/LATTEX, Faculdade de Ciências da Universidade de Lisboa, Campo Grande, Ed. C2, 5° piso, 1749-016 Lisboa, Portugal

[7] Geotransfer (Instituto Universitario de Ciencias Ambientales de Aragón), Universidad de Zaragoza, 50009 Zaragoza, Spain

[8] Departamento de Geociências, Universidade de Aveiro, 3810-193 Aveiro, Portugal

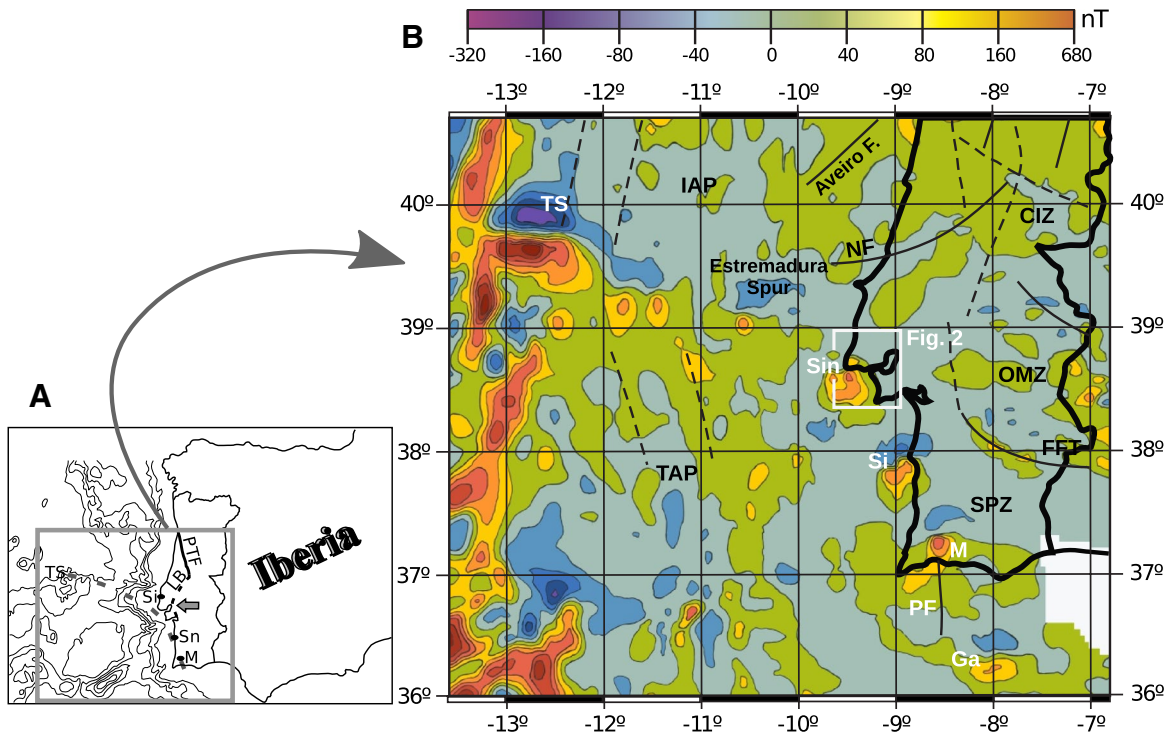
A
Iberia
TS
PTF
IAP
Si
Sn
M
B
nT
-320
-160
-80
-40
0
40
80
160
680
-13º
-12º
-11º
-10º
-9º
-8º
-7º
40º
39º
38º
37º
36º
TS
IAP
Aveiro F.
CIZ
NF
Estremadura Spur
Fig. 2
Sin
OMZ
Si
FFT
TAP
SPZ
M
PF
Ga

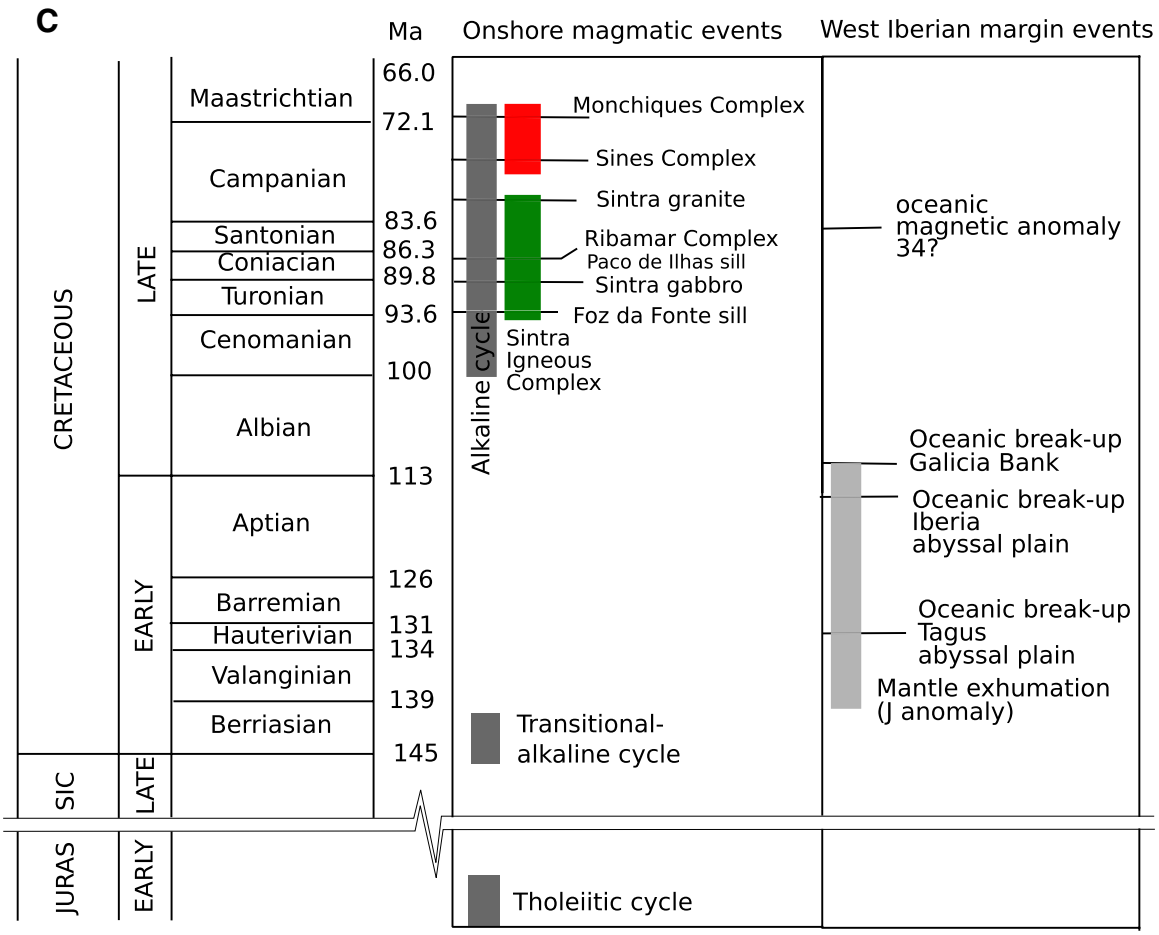
C
Ma
Onshore magmatic events
West Iberian margin events
CRETACEOUS
JURAS
LATE
EARLY
SIC
Maastrichtian
Campanian
Santonian
Coniacian
Turonian
Cenomanian
Albian
Aptian
Barremian
Hauterivian
Valanginian
Berriasian
66.0
72.1
83.6
86.3
89.8
93.6
100
113
126
131
134
139
145
Monchiques Complex
Sines Complex
Sintra granite
Ribamar Complex
Paco de Ilhas sill
Sintra gabbro
Foz da Fonte sill
Alkaline cycle
Sintra Igneous Complex
Transitional-alkaline cycle
Tholeiitic cycle
oceanic magnetic anomaly 34?
Oceanic break-up Galicia Bank
Oceanic break-up Iberia abyssal plain
Oceanic break-up Tagus abyssal plain
Mantle exhumation (J anomaly)

◂**Fig. 1** **a** Location of the study area in the West Iberian Margin. **b** Magnetic anomalies of the Western Iberian margin and location of the Sintra (Sin), Sines (Si) and Monchique (M) Late Cretaceous Alkaline Complexes. Note the lineament formed by the magnetic anomalies, and also the anomaly larger than the Sintra Complex located to the south in the offshore nearby. *Ga* guadalquivir seamount anomaly, *IAP* Iberia Abyssal Plain, *TS* tore seamount anomaly, *TAP* Tagus Abyssal Plain, *NZ* Nazaré Fault, *PF* Portimão Fault, *CIZ* Central Iberian Zone, *OMZ* Ossa-Morena Zone, *SPZ* South-Portuguese zone. **c** Main magmatic and plate-scale events in the Western Iberian Margin during the Mesozoic (see text for further explanation)

Intrusive bodies in intra-plate, anorogenic settings show a variety of geometries, often conditioned by the mechanical stratigraphy of the pre-existing sedimentary sequence (e.g., Román-Berdiel et al. 1995b, 1997, and references therein; Calvín et al. 2017). The existence of décollements within the sedimentary pile often favours the development of tabular or laccolith-shaped bodies (e.g., Rocchi et al. 2002), whose internal structure can be conditioned either exclusively by flow mechanics (lateral expansion of magma) or by a combination of the latter and the tectonic stress field (Paterson et al. 1998).

The western Iberian passive margin shows a suite of intrusive complexes related to its Late Cretaceous evolution (Rock 1982; Miranda et al. 2009). These intrusions (Sintra, Sines, and Monchiques, from North to South) depict elliptical, E–W elongated outcrop areas, and define an NNW–SSE lineament (Figs. 1, 2). On the magnetic anomaly map of Portugal and adjacent offshore areas, these intrusions stand out as strong anomalies that are aligned with a fourth one located on the Guadalquivir Bank, thus forming a 300 km-long lineament (Fig. 1, Silva et al. 2000).

The Sintra Igneous complex (SIC), is one of the most prominent and interesting bodies within this system, comprising intrusive bodies of gabbro, syenite, granite, and various suites of dykes and sills. However, a detailed study to unravel the magma emplacement model and its relationship with the surrounding tectonic structures has not yet been developed. The aim of this paper is to define its internal structure and 3D geometry and to shed some light on its emplacement mode and its tectonic controls/style. These two goals are attempted by means of three new data sets—structural, anisotropy of magnetic susceptibility (AMS), and gravity modeling. The combination of magnetic fabrics with the geometrical reconstruction derived from gravimetric studies (provided that density contrasts exist between the igneous bodies and the host rocks) and structural data allow a reliable approach to the tectonic links of this singular intrusion.

Regional geology

The West Iberia Margin, together with the Bay of Biscay and the Gulf of Cadiz, was structured during the Mesozoic rifting (Early Triassic through Early Cretaceous, e.g., Montenat et al. 1988; Wilson et al. 1989; Stapel et al. 1996; Rasmussen et al. 1998; Kullberg 2000; Alves et al. 2006; Kullberg et al. 2013) leading to the break-up of Pangea and the formation of a series of N–S aligned sedimentary basins (Fig. 2). Oceanic break-up occurred at 132 ± 1.9 Ma (Late Valanginian /Early Hauterivian) in the Tagus Abyssal Plain, ~ 126 Ma (Early Barremian) in the Iberia Abyssal Plain and 112 ± 1.1 Ma in the Galicia Bank (Pinheiro et al. 1996; Tucholke et al. 2007). Alternatively, Bronner et al. (2011) proposed that mantle exhumation occurred from ~ 140–112 Ma, accounting for the J magnetic anomaly (Fig. 1). This was accompanied by a phase of magmatic underplating and production of alkaline intrusions along the Madeira-Tore Rise and J anomaly of Iberia during the Cretaceous. According to these authors, the age of the first clear oceanic anomaly is ~ 84 Ma, i.e., (Santonian, Late Cretaceous). From the Sintra Igneous complex (SIC) to the west towards the Atlantic Ocean, a series of magnetic anomalies (Fig. 1b) define a W–E lineament (Neres et al. 2014) associated with a set of west–east trending dyke and sill system interrupted by volcanic cones.

The study of onshore igneous rocks allowed to establish three cycles of Mesozoic magmatic activity separated by intervals of ~ 50 Ma (Fig. 1c): (i) an Early Jurassic tholeiitic basaltic cycle, coeval with the beginning of the Central Atlantic opening, with ages around 200 Ma (Verati et al. 2007; Martins et al. 2008), (ii) a transitional-to-mildly alkaline cycle, consequence of the lithospheric thinning related to the Atlantic opening, that took place during the Jurassic–Cretaceous transition (148–140 Ma, Martins 1991; Grange et al. 2008; Mata et al. 2015), and (iii) a Late Cretaceous alkaline cycle (100–70 Ma, Miranda et al. 2009; Grange et al. 2010; Neres et al. 2014).

The Late Cretaceous alkaline igneous province of Portugal includes the NNW–SSE aligned intrusive complexes of Sintra, Sines and Monchique, the Ribamar diorite, the Lisbon Volcanic Complex, and the Mafra Radial Dyke Complex, as well as small and scattered sub-volcanic intrusions (Fig. 2). Miranda et al. (2009) divided the alkaline magmatic activity in two pulses. The first, older pulse, during which the SIC was emplaced, has a wider geographical distribution and more diverse modes of occurrence such as sub-volcanic complexes, flows, vents, plugs, dykes, and sills. It occurred during the opening of the Bay of Biscay and the resulting counter-clockwise rotation of Iberia (94–80 Ma). The Sines and Monchique intrusions were emplaced during the second pulse between 75 and 72 Ma.

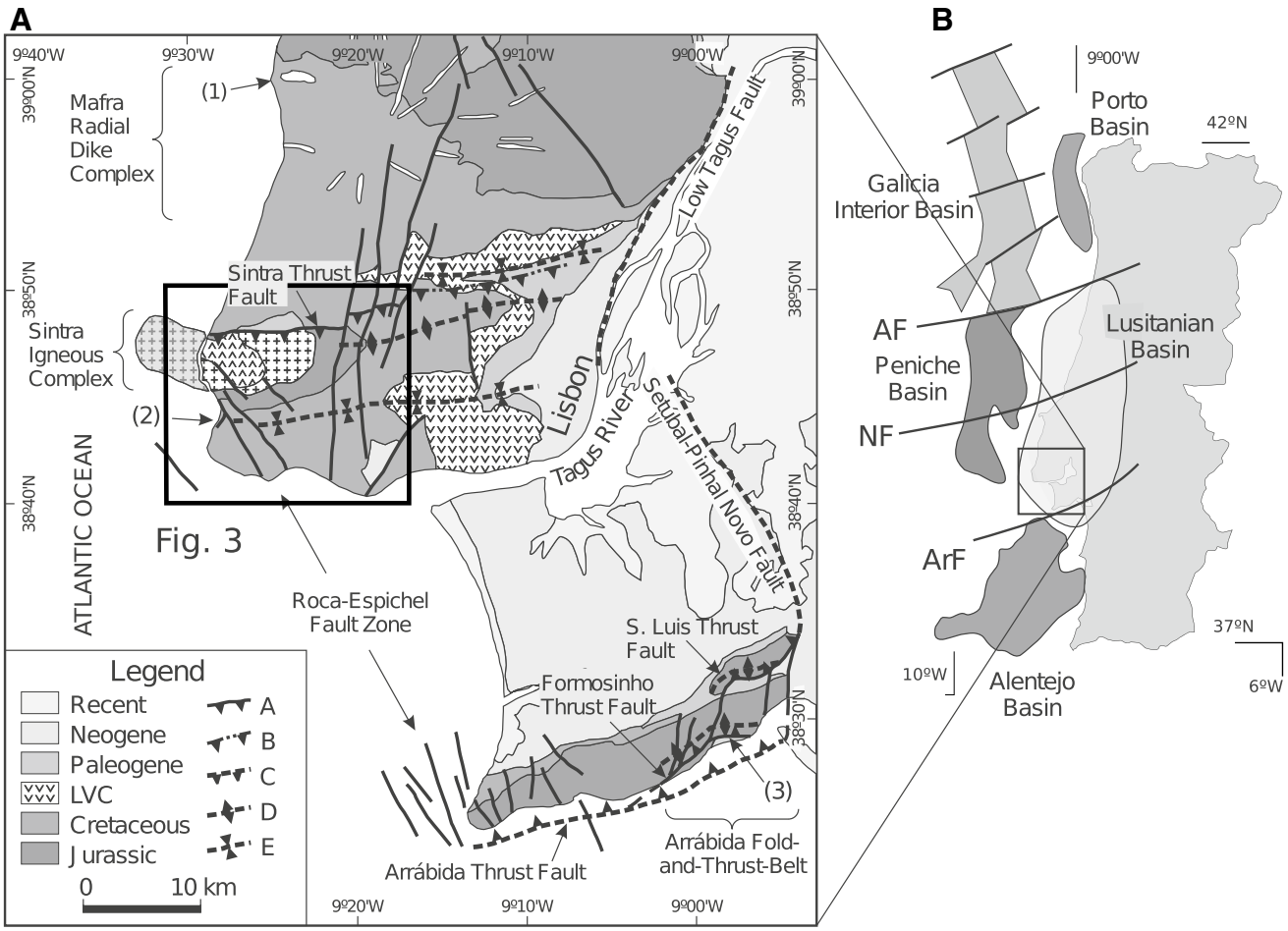

Fig. 2 Structural map of the southern part of the Lusitanian Basin. Note that the Roca-Espichel Fault Zone (REFZ) was extensional during the Jurassic rifting and acted as a dextral strike-slip during the Late Cretaceous and Paleogene tectonic inversion in the Sintra–Lisbon region and during the Early–Middle Miocene in the Arrábida fold-and-thrust-belt. Abbreviations for the Legend: *LVC* Lisbon Volcanic Complex, *A* thrust fault, *B* blind thrust fault, *C* inferred thrust fault; *D* anticline; *E* syncline Abbreviations for the map: (1) Paço de Ilhas sill; (2) and (3) Syn-rift normal faults (Kimmeridgian and Bajocian, respectively); *MRDC* Mafra Radial Dike complex, *SIC* Sintra Igneous complex, *AF* Aveiro fault, *NF* Nazaré fault, *ArF* Arrábida fault

The Sintra Igneous complex in its structural setting

The onshore part of the SIC has an area of about 50 km^2 depicting an elliptical E–W elongated outcrop of granite (10.5×5.5 km) that intrudes the Upper Jurassic (Fig. 3). The offshore part of the SIC is estimated to be approximately equal to the onshore one (Fig. 2). In the middle of the granite, an NNW–SSE trending sub-elliptical complex of syenite, gabbro, diorite, and intrusive multi-compositional breccias crop out (Alves 1964). Scattered gabbros also crop out along the northern thrust of the SIC. These intrusive bodies are accompanied by sills, cone-sheets, and ring-dykes of varied compositions and orientations (Fig. 3). Granite facies consist mainly of quartz and feldspar (Fig. 4) and lack solid-state deformational structures, although undulose extinction can be rarely seen in quartz grains. Gabbro, where brittle structures are frequent (Fig. 4), includes plagioclase, biotite, pyroxene, and opaque minerals (probably magnetite, also present in some specimens of granite). Syenite facies show plagioclase with porphyritic, microcrystalline texture in some cases (Fig. 4). The abundance of opaque minerals within the syenite and gabbro facies (and also in some of the granite samples) is probably related to their magnetic behavior (i.e., many samples attract common Nd magnets).

Recent geochronological data based on U–Pb zircon ages, indicate that the Sintra granite is slightly younger than the gabbro body of the SIC, and yield an ambiguous chronological relationship between granite and syenite: Miranda et al. (2009) obtained ages of 79.2 ± 0.8 Ma for the granite and Grange et al. (2010) obtained an age of 81.7 ± 0.4 Ma age for the granite, 80.1 ± 1.0 Ma for micro-syenite, and a robust 83.4 ± 0.7 Ma age for the gabbro bodies. These latter authors fixed alkaline magma emplacement in the

Western Iberian Margin between 88 and 68 Ma showing a north–south age trend: Ribamar (88 Ma), Sintra (83–80 Ma), Sines (77–76 Ma), and Monchique (70–69 Ma).

The present-day structure of the SIC is the result of several deformation events including (i) the Mesozoic rifting stage of the Lusitanian Basin (LB), (ii) deformational structures linked to magmatic intrusions, and (iii) thrusts and strike-slip faults associated with the tectonic inversion of the LB during the Cenozoic. Because of their relationships with magmatic bodies or syn-tectonic deposits, many structures can be ascribed to one of these stages, as follows.

Inversion structures

The onshore outcrop of the SIC is surrounded by an asymmetric rim syncline with an overturned flank of Upper Jurassic and Lower Cretaceous overthrust by the SIC towards the north. This thrust zone extends into the offshore for an uncertain distance and eastwards up to the Tagus river where it becomes a blind thrust (Figs. 2, 3). Altogether, it forms an ENE–WSW northwards directed, > 50 km-long thrust zone. The thrust displacement decreases eastwards away from the SIC both gradually and by discrete attenuation through N–S-striking transfer faults. The age of thrusting is not well constrained due to the poor dating of the continental conglomerates and other terrigenous deposits that are also overthrust by the SIC. According to Carvalho (1994), these deposits of Paleogene age can be as old as Eocene. The net angular unconformity of sub-horizontal Lower Miocene marine deposits on top of folded Paleogene formations is a clear indication of pre-Miocene folding and thrusting. Eocene thrusting is in agreement with fission track ages at 57 Ma for uplift obtained from apatites of the granite of the SIC (Stapel 1999). The thrusting in the Sintra–Lisbon area was only slightly re-activated during the Miocene, when regional shortening concentrated in the Arrábida fold-and-thrust-belt during Burdigalian and Langhian times (Fig. 2, Ribeiro et al. 1979, 1990; Kullberg et al. 2000).

Aerial-photo interpretation of the SIC and surrounding country rocks revealed the occurrence of NE–SW and NW–SE trending lineaments, not evident in the field (outcrop scale), where they form prominent valleys, due to the dense forest and a thick soil cover. However, at the southern and south-western contacts with the sedimentary host rocks, the map pattern points to strike-slip movements on conjugate faults, consistent with an N–S compression direction. The latter is compatible with (i) outcrop scale kinematic indicators, such as slickensides on folded strata and striae on the NW–SE trending faults and (ii) regional scale indicators, such as the E–W strike of the northwards directed Sintra Thrust and the N–S strikes of the transfer faults that attenuate the Sintra Thrust towards the East (Fig. 2).

Rift tectonics

Only a few pre-tectonic inversion structures were clearly identified due to the dominant compressive overprint. However, NE–SW trending extensional faults within the Oxfordian hemipelagic marls and limestone debris flows (Fig. 5a), as well as E–W trending faults within the Lower Cretaceous shallow water marine limestones, were observed. These faults are cross-cut by dykes of the SIC, which attest to their pre-intrusion age. During the tectonic inversion, they were either passively rotated on the southern limb of the rim syncline or re-activated as major and/or as secondary NW–SE and NE–SW conjugate strike-slip faults (Neves et al. 2009). Clear evidences for syn-rift activity of the NW–SE trending faults can be found at the Arrábida fold-and-thrust-belt, 30 km south of the SIC (Fig. 2). In this area, NW–SE faults bound half-grabens containing sedimentary growth wedges of Middle Jurassic age (Kullberg 2000). The NW–SE faults were passively carried on top of the ENE–WSW trending thrusts (e.g., S. Luis Thrust Fault in Fig. 2) and abut against a major E–W trending basin boundary transfer fault (Arrábida Thrust Fault in Fig. 2), the southern tectonic boundary of the LB.

It can, therefore, be argued that the E–W trending frontal thrust at the front of the SIC results from the tectonic inversion of pre-existing extensional faults based on the following: (i) the presence of a package of debris flow consisting of shelf carbonates interlayered with hemipelagic black marls of Oxfordian age (~ 200 m thick) only to the south of the E–W trending northwards directed thrust (Fig. 5a), whilst to the north of this fault, only coeval shelf carbonates exist; and (ii) the presence of E–W trending extensional faults, at both the outcrop and map scales, and sedimentary growth wedges in the Lower Cretaceous on the southern edge of the SIC.

Tectonics and relative chronology of intrusions

The emplacement of the SIC is associated with (i) formation of intrusive breccias, (ii) ductile deformation of the host rocks during intrusion, and (iii) brittle fracturing of the host rocks. The igneous breccias are always found either within the gabbro–diorite–syenite or at the contact of this intrusion with the granite (Alves 1964). The sills and the host rocks were stretched during the intrusion of the SIC. The sills show extensional domino-like structures near the contact with the granite (Fig. 5b); the host Oxfordian carbonates display thermal metamorphism, semi-ductile extensional faults, extreme flattening of blocks and pebbles from conglomerates and debris flow layers, and a pervasive set of fissures, which are perpendicular to bedding and their strike is parallel to the contact with the granite. These fissures color the black marls in white, giving them a zebra-like pattern that results

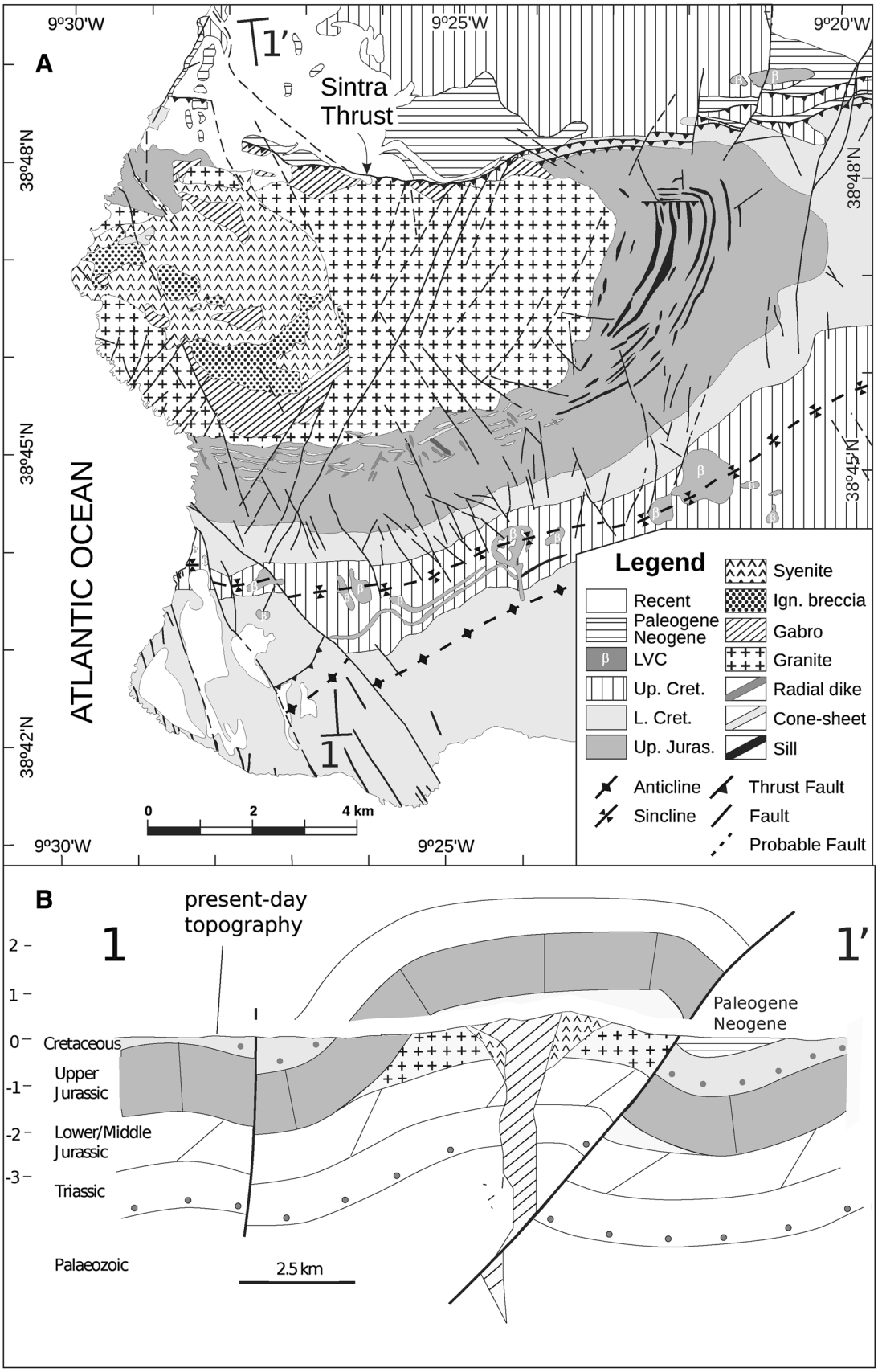
A
9°30'W
9°25'W
9°20'W
38°48'N
38°45'N
38°42'N
1'
1
Sintra
Thrust
ATLANTIC OCEAN
0
2
4 km
Legend
Recent
Paleogene
Neogene
LVC
Up. Cret.
L. Cret.
Up. Juras.
Syenite
Ign. breccia
Gabro
Granite
Radial dike
Cone-sheet
Sill
Anticline
Sincline
Thrust Fault
Fault
Probable Fault
B
present-day
topography
1
1'
2
1
0
-1
-2
-3
Cretaceous
Upper
Jurassic
Lower/Middle
Jurassic
Triassic
Palaeozoic
Paleogene
Neogene
2.5 km

◂**Fig. 3** **a** Geological map of the SIC and surroundings. The Upper Jurassic limestones at contact with the igneous rocks dips ~ 70° on the normal limb of the syncline and is overturned along the northern contact. Cone-sheets dip towards the gabbro–syenite intrusion. **b** Simplified cross section of the Sintra complex and the host rocks based on data presented in this work

from reaction of oxidizing fluids exhaled from the intrusion (Fig. 5c).

The sills of micro-gabbro, dolerite, or lamprophyre are found only in the sedimentary host rock and, consequently, no cross-cutting relationships were observed between the sills and the granite. They occur profusely along the eastern side of the SIC and are less common on its southern flank where they are cross-cut by the ring-dykes and the cone-sheets. Two of them are dated, the Paço de Ilhas sill (Fig. 2), 88.0 ± 2.2 and 86.8 ± 2.5 Ma (K–Ar on biotite and K-feldspar, respectively, Mahmoudi 1991) and Foz da Fonte sill, 93 Ma (^{40}Ar–^{39}Ar on amphibole, Miranda et al. 2009).

The cone-sheets consist of dykes of varied composition, often felsic, and are restricted to the central part of the southern flank of the SIC. They dip towards the north and northwest, i.e., towards the gabbro–syenite intrusion. Cross-cutting relations show that the sills predate the cone-sheets. The radial dykes are less common than the latter, generally mafic and altered. They cross cut the cone-sheets and the sills, and occur along the southern and northern central parts of the SIC (Fig. 5d).

Gravimetric data

Gravimetric anomalies

About 160 new gravity measurements were taken, using a Lacoste and Romberg model G gravity meter, covering an area of ~ 150 km^2 (Fig. 6). Within the massif, the spacing of gravity stations is between 0.5 and 1 km. Outside the SIC, several radially arranged traverses apart from each other were completed, with similar spacing between stations along each traverse. Elevation at stations was determined either from fixed elevation marks in maps (scale 1:25,000) and/or with a barometric altimeter with an accuracy of 0.5 m, such that an accuracy of ~ 0.2 mGal can be ascertained for the gravity survey. The Bouguer anomaly map was computed using a mean value of 2600 kg m^{-3} for the density, taking into account the density of the rocks. Topographic corrections up to a distance of 28 km were applied to all stations. Since no absolute reference was available, our gravity data are relative measurements with respect to the base, located at sea level in the north-western part of the study area (Fig. 6). The total amplitude of the measured gravimetric field with respect to this origin varies between − 15 and + 6 mGal, these extreme values being obtained in the northeast and southwest of the study area, respectively (Fig. 6a).

The Bouguer anomaly map (Fig. 6a) shows an NNW–SSE regional trend, clearly outlined outside the outcrop limits of the SIC. Within the massif, and near its northern border, deflection toward the west of the Bouguer anomaly contours comes from the lower density of the syenitic and granitic bodies with respect to the country rocks. In the southwest of the massif, a gravity high, along with strongest gradients, coincides with the largest outcrops of gabbroic facies. Regional contours are also strongly deflected in the footwall of the Sintra thrust, where the Cenozoic sandstones and lutites crop out, suggesting the prolongation of the low-density igneous body below the sedimentary cover.

The regional gravity anomaly of the Iberian Atlantic Margin is conditioned by the trend of the margin and the westward thinning of the continental crust. It consists of a regularly NNW–SSE trending surface dipping to the northeast (Mezcua et al. 1996), with an approximate gradient of about 1.5 mGal km^{-1}. A cubic surface following this trend was obtained from the Bouguer anomaly map. The zero contour line of the residual anomaly map (Fig. 6b) is roughly parallel to the northern boundary of the SIC. The residual anomaly displays mean values of − 0.5 to − 3 mGal in most of the massif, and negative anomalies up to − 4 mGal are observed to the north of the Sintra thrust. The gravity high with a northward-opened crescent shape up to + 3.5 mGal, slightly shifted to the East with respect to the limit between gabbro and the syenite to the south, is also clearly outlined.

Gravimetric modeling

Gravimetric modeling (2.5-D) of the residual anomaly was done with the program Gravmag from the British Geological Survey (Pedley 1991). The densities of the igneous rocks were determined from 410 measurements of rock samples with an accuracy of ~ 5 kg m^{-3}. They vary from 2400 kg m^{-3} (granite) to 2820 kg m^{-3} (gabbroic facies), with an arithmetic mean of 2570 kg m^{-3} for the whole of the measured samples (2540 kg m^{-3} for the granitic facies, 2590 for the syenite and 2740 for the gabbroic facies, on average, Fig. 7). Since the number of samples is related to the areal distribution of the different facies and because of the even sampling carried out, these values can be considered as representative for the different parts of the igneous body. The density of the host rock, made of Upper Jurassic marine limestones is 2700 kg m^{-3}, on average. Basic dykes that intrude the Jurassic limestones close to the SIC have shown densities of 2870 kg m^{-3}. Finally, Cretaceous and Cenozoic rocks cropping out to the north and south of the massif have densities of 2650 and 2600 kg m^{-3}, respectively.

Five NNW–SSE trending geological and gravity sections (located in Fig. 5b) were undertaken (Fig. 7). Negative

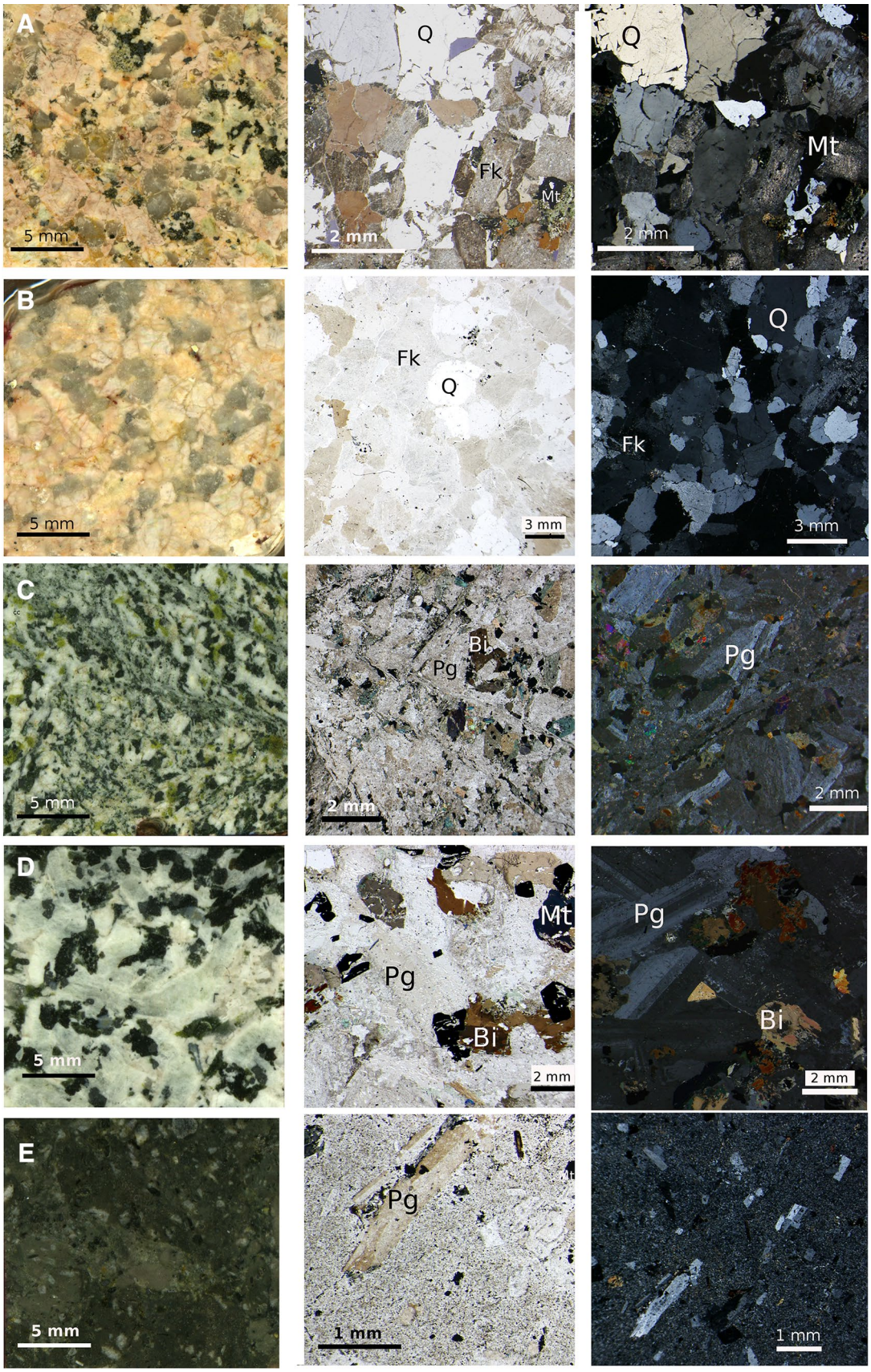
A
5 mm
Q
Fk
Mt
2 mm
Q
Mt
2 mm
B
5 mm
Fk
Q
3 mm
Q
Fk
3 mm
C
5 mm
Bi
Pg
2 mm
Pg
2 mm
D
5 mm
Mt
Pg
Bi
2 mm
Pg
Bi
2 mm
E
5 mm
Pg
1 mm
1 mm

◂**Fig. 4** Polished sections under reflected light (left column) and thin sections under parallel (middle column) and crossed polarizers (right column) of several lithotypes of the SIC: magnetite-bearing granite, site S-8 (**a**), granite, site S-32 (**b**), gabbro showing brittle deformation, site S-36 (**c**), non-deformed gabbro, site S-2 (**d**), micro-syenite with phenocrysts, site S-13 (**e**). *Pg* plagioclase, *Fk* K-feldspar, *Q* Quartz, *Mt* probably magnetite

residual anomalies within the massif are explained by the lower density of the granite and syenite with respect to the country rock. The densities of the granite and syenite are similar and, therefore, they cannot be distinguished based on the gravimetric data only. However, because of their geological implications, in the models shown in Fig. 7, these two bodies are distinguished, and the contacts between them are traced according to surface geology. According to the information about depths to the base of the different igneous bodies obtained from the cross sections, maps showing the geometry of the different igneous bodies were traced (Fig. 8). As discussed in the "Interpretation and Discussion" section, the gabbro body shows several root zones aligned in E–W direction, whereas the syenite and granite intrusions can be characterized as laccoliths whose size slightly exceed the outcropping limits of the igneous body.

Anisotropy of magnetic susceptibility

Anisotropy of magnetic susceptibility (AMS) has proven to be a fair indicator of the magmatic/tectonic fabric of igneous bodies (Bouchez et al. 1990; Román-Berdiel et al. 1995a, b; Aranguren et al. 1996; Bouchez 1997; Neres et al. 2014), both in para- and ferro-magnetic lithologies (Archanjo et al. 1995). AMS analysis is a powerful tool to identify structural patterns in magmatic rocks, especially in those displaying poor evidences at the outcrop scale (e.g., Graham 1954; Tarling and Hrouda 1993; Borradaile and Henry 1997; Borradaile and Jackson 2010). In particular, this technique helps understanding the mineral fabric (preferred orientation), hence the flow (magmatic fabric) or deformational structures (solid-state fabric) in granitic bodies (Bouchez 1997, 2000). Associated with detailed structural maps and gravimetry surveys, AMS sheds light constraining shapes of emplacement modes of plutons, as exemplified in this work.

The parallelism between the crystallographic axes of some minerals, especially phyllosilicates (Borradaile and Werner 1994; Martín-Hernández and Hirt 2003), allows achieving the mineral fabric in a simple and fast way, particularly when the iron-bearing silicates are the main magnetic contributors (Rochette 1987; Rochette et al. 1992). The mineral and magnetic fabric correspondence has been double-checked by various methods including: image analysis (Launeau 1990), experimental modeling (Arbaret et al. 1995), or structural data (Román-Berdiel et al. 1995a, b; Archanjo et al. 1995; Aranguren et al. 1996; Román-Berdiel and Pueyo-Morer 2000).

Geological interpretations of AMS fabrics are more straightforward when the para-magnetic mineral contribution is larger than the ferro-magnetic one (Rochette et al. 1992; Pueyo-Anchuela et al. 2013). Non-magnetic granites, i.e., belonging to the ilmenite-series of Ishihara (1977), with susceptibilities from 10^{-5} to 10^{-4} S.I. (Ellwood and Wenner 1981), usually display a dominant para-magnetic susceptibility (Gleizes et al. 1993; Leblanc et al. 1994; Román-Berdiel et al. 1995a, b), and their magnetic ellipsoids exhibit a clear correlation with the mineral preferred orientation. In magnetite-bearing granites, with susceptibilities ranging from 10^{-3} to 10^{-2} S.I., the directional correspondence between the AMS and the crystalline anisotropy has been also proven (Grégoire et al. 1995, 1998; Pignotta and Benn 1999).

Sampling and laboratory procedures

Our AMS sampling concerns 54 new sites evenly distributed throughout the outcropping area of the SIC (Fig. 9; Table 1, see Appendix 1 for stereoplots of individual sites). In each site, 3–4 cores were obtained with a portable drilling machine. Samples were in-situ oriented with a special compass directly in the field. In a few cases (gabbroic facies), the orientation was double-checked with a solar orientator.

The magnetic anisotropy of 409 standard cylinders (2.5 cm in diameter, 2.1 cm in height) was measured at low field with a KLY-2 susceptometer (Agico, Ltd.) at the Geology Department of the Universidad del País Vasco-Euskal Herriko Unibertsitatea (Bilbao). From each site, about eight specimens (when possible) were measured to ensure enough quality of the site-means (Pueyo et al. 2004). Magnetic mineralogy was controlled by means of susceptibility-temperature, *k*–*T* curves in representative specimens of the three lithologies at the magnetic fabrics laboratory of the University of Zaragoza. To separate the para-magnetic and ferro-magnetic contributions, some high field and hysteresis measurements up to 1 T (Fig. 10) were conducted at room temperature in samples representative of the different rock types, using an MPMS magnetometer (Quantum Design Ltd.) at the Institute of Material Sciences of Aragon (ICMA, CSIC-University of Zaragoza). Additional hysteresis loops and back field experiments were carried out to characterize the magnetite grain size in an MVSM magnetometer (by Lakeshore) in the laboratory of the Zentralanstalt für Meteorologie und Geodynamik (Wien, Austria).

The orientations of mean susceptibility axes (K_{max}, K_{int}, and K_{min}) were adjusted using a symmetric Bingham (1974) distribution as proposed by Román-Berdiel et al. (1995a, b). Its accuracy was characterized (Table 1) by the magnitude of the first eigenvector ($E1$) along with the β angle ($=\tan^{-1}[E1/E2]$) of Pueyo et al. (2004), and the lineation

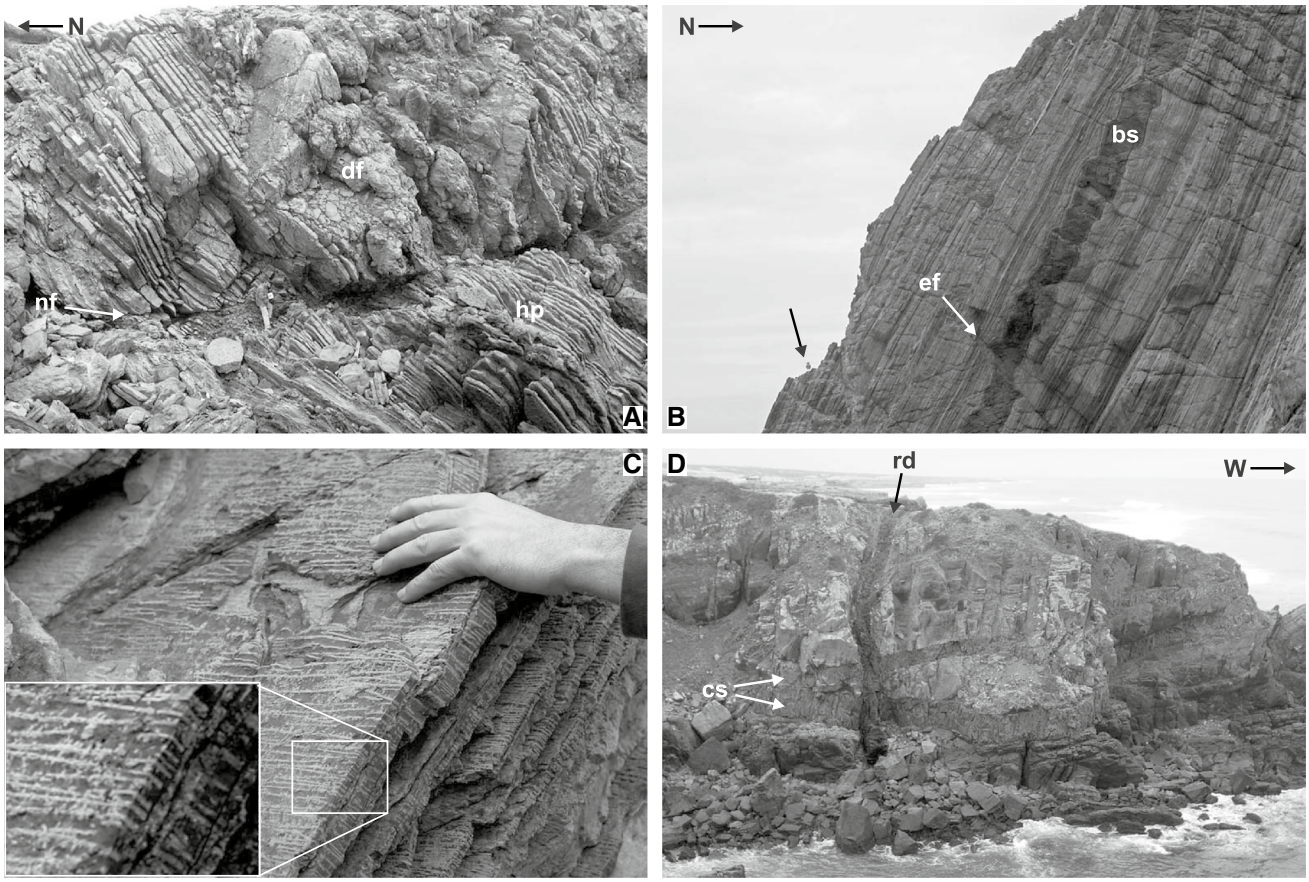

Fig. 5 Mesoscale structures affecting the sedimentary country rock near the southern limit of the Sintra Igneous complex: **a** tilted Late Jurassic normal fault (nf) cross-cutting the Upper Jurassic hemipelagic black marls (hp) and shelf debris flows (df) (geologist for scale); **b** extensional structures caused by early intrusion stages, basic sill (bs) showing extensional domino structures and overturned semi-ductile extensional faults (ef) in the Upper Jurassic sediments (seagull for scale, black arrow); **c** metasomatic veins, perpendicular to bedding, oxidizing the Upper Jurassic black shales (view toward the south), and **d** radial dykes (rd) cross-cutting the cone-sheets (cs). For location of outcrops, see Fig. 3

and foliation significance was evaluated using quality criteria (op. cit.); for example, lineation orientation is not reliable when Jelinek's (1981) angle $E_{12} > 25°$, since K_{max} is almost undifferentiated from K_{int}.

Magnetic mineralogy and spatial distribution of the bulk susceptibility

The bulk susceptibility values (Table 1; Fig. 10), ranging between 3.9×10^{-5} and 7.2×10^{-2} S.I. show a remarkable difference between the two magmatic bodies forming the SIC (Fig. 10a, b). The granite displays medium-to-low susceptibility values, partially falling within the "non-magnetic" field, with the exception of a few sites (close to the gabbro–syenite). On the contrary, the gabbro–syenite body has much higher susceptibilities mostly within the "magnetic" type. Along with the drilling, susceptibility was directly measured in the field (using a KT-6 susceptometer, Satisgeo Ltd.). Site-means based on 7–9 in situ measurements have been compared with those derived from the KLY-2 (Fig. 10c). The high degree of correlation and the efficiency of these measurements make this kind of instruments very suitable to increase the density and quality of bulk susceptibility mapping.

Thermomagnetic (k–T) curves having positive slope (Fig. 11a) indicate that ferro-magnetic (S.l.) minerals are the main contributors to susceptibility in the three analyzed rock types. Curie temperatures of ferro-magnetic (S.l.) minerals indicate that magnetite is the main (and probably only) phase, as also inferred from the other experiments performed. Other minor components with lower Curie temperatures are iron sulphides. Interestingly, bulk susceptibility depends strongly on the presence of magnetite crystals in particular samples (these crystals can be observed under the microscope, Fig. 4), and, therefore, this factor must be taken into account when correlating petrographic facies and bulk magnetic susceptibility.

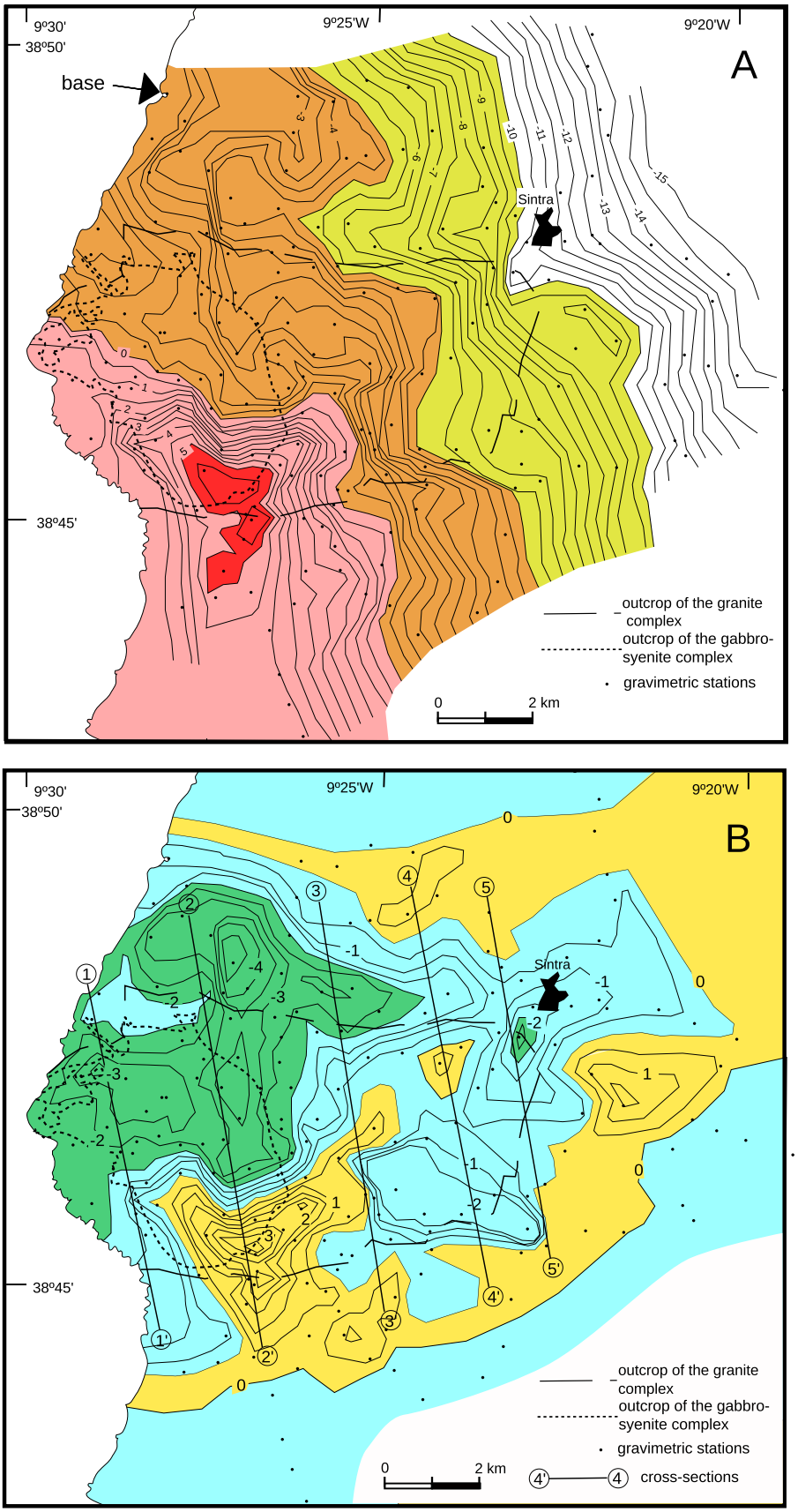

Fig. 6 Gravity anomaly maps of the SIC and surrounding area: **a** Bouguer anomaly map obtained from gravity measurements obtained in this work; **b** residual anomaly map obtained from the gravimetric survey. Contours in mGals correspond to relative values of gravity, with respect to the base located in the northwest of this map. Contour interval 0.5 mGal. The dashed lines correspond to the outcrop limits of the SIC. Points are gravimetric stations measured in this study. Cross sections: see Fig. 7

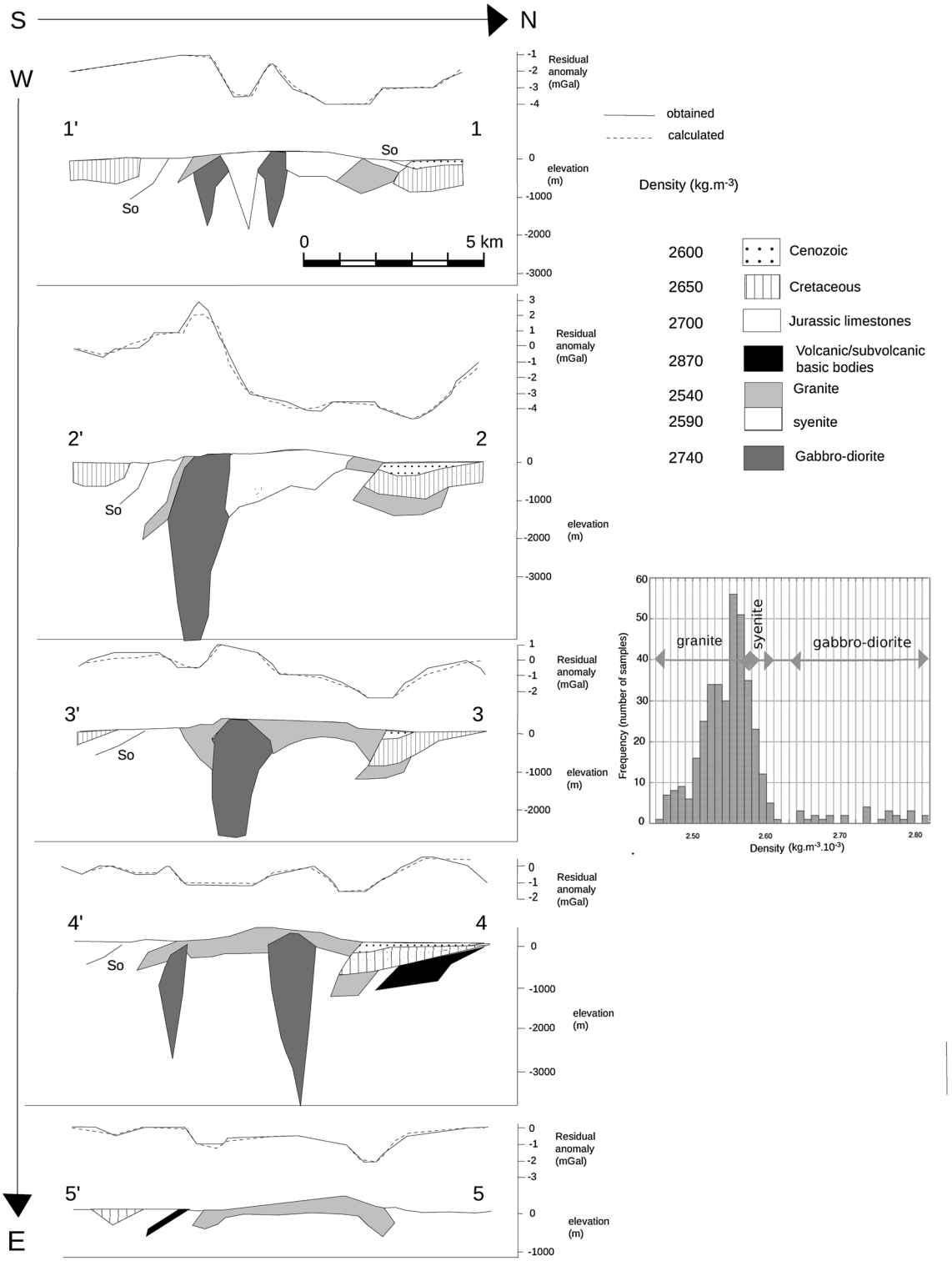

Fig. 7 Gravimetric modeling of the SIC, combining geological and gravimetric data. See location of cross sections in Fig. 6b. The densities considered are indicated by vertical bars in the histogram with the same patterns shown in the cross sections. The Quaternary sands were modeled with a thickness of several meters in the upper part of the sections but are not visible at this scale. The limit between the granitic and syenitic bodies is not derived from gravimetric modeling, since their densities are very similar, but interpreted according to surface geology and is, therefore, uncertain at depth

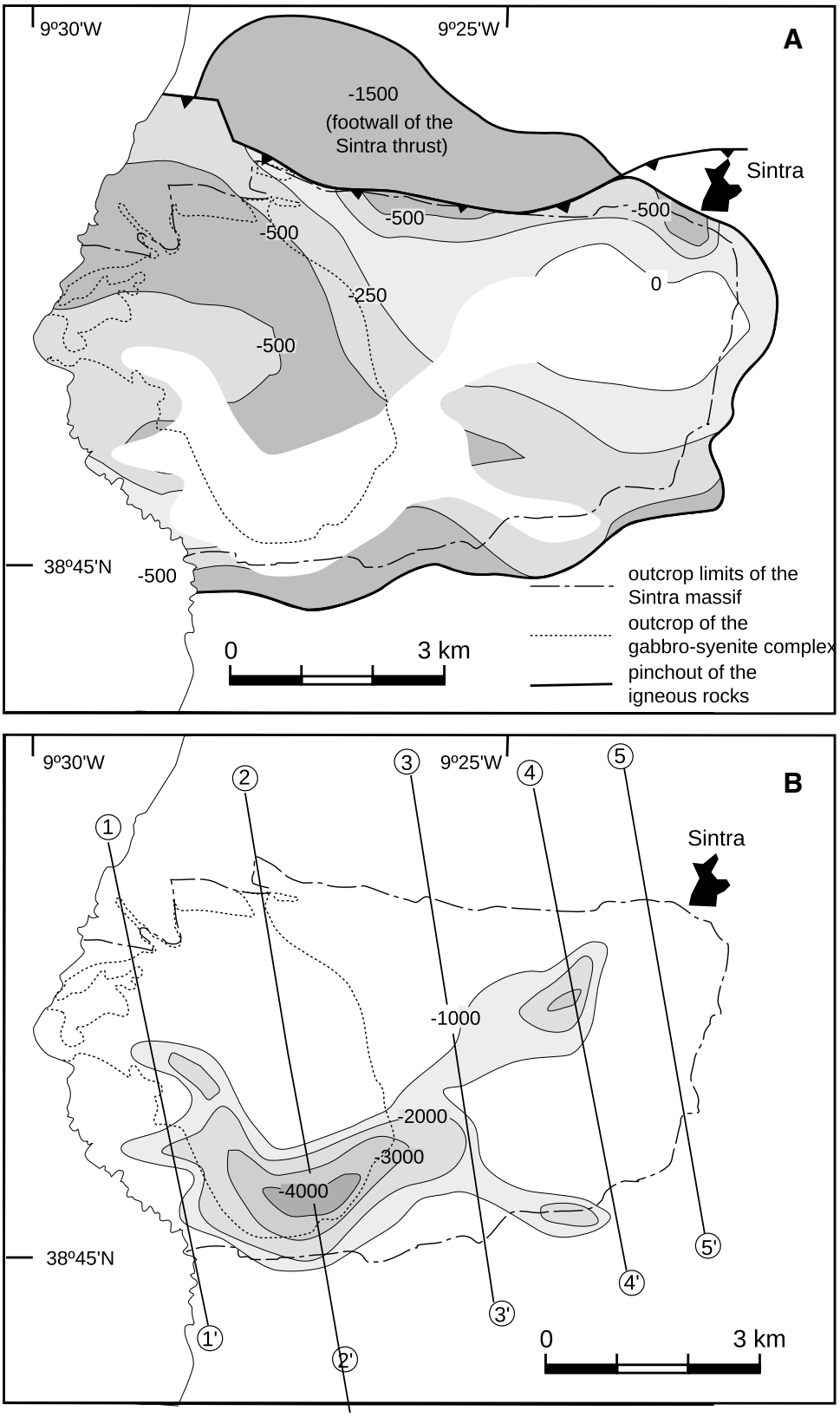

Fig. 8 Depth contours of the igneous bodies defining the SIC (in meters). Although the syenitic body is genetically related with gabbros and not with the granite, granite and syenite were grouped because of the difficulty of separating them by density difference. These maps must then be considered as defining "density" bodies and not "genetic" bodies. **a** Contours for the bottom of the low-density felsic laccoliths (syenite and granite) obtained from gravimetric modeling. The area in white corresponds to the cross-cutting of this body by the steeply dipping walls of the gabbro plugs. **b** Contours of the high-density gabbro plugs D rawn from the gravimetric cross sections and taking into account the residual anomaly map

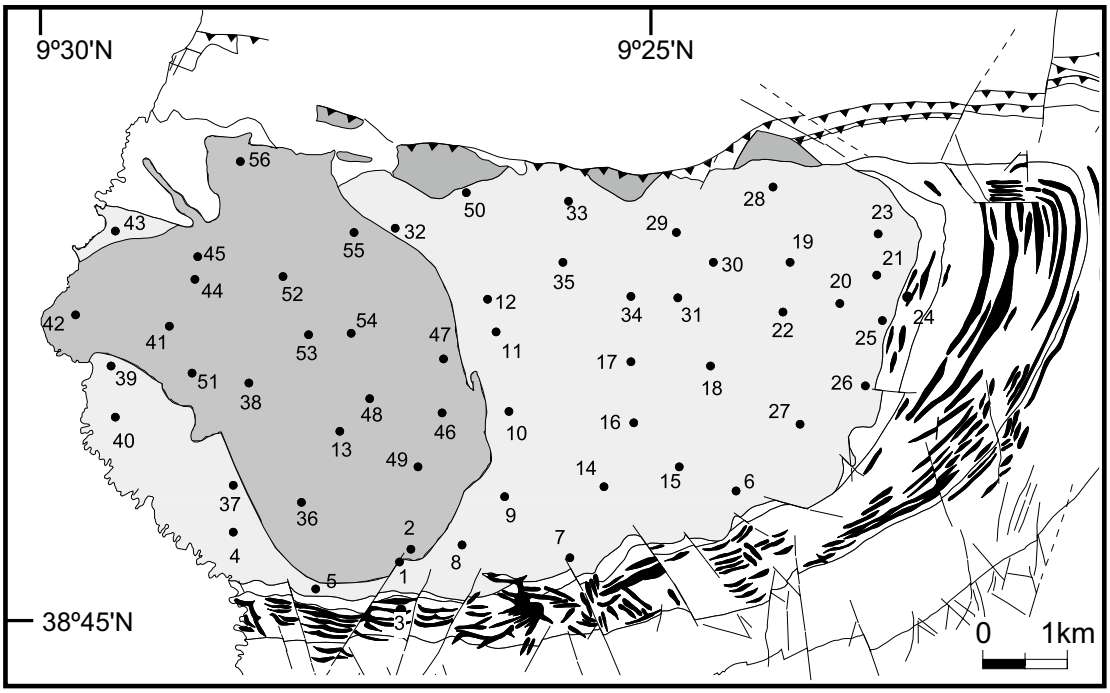

Fig. 9 AMS sampling design in the Sintra Massif (see coordinates of sites in Table 1). Directional results from individual sites are shown in Appendix 1

Hysteresis loops (Fig. 11b), carried out in a few samples covering the wide range of susceptibilities, point to the occurrence of low coercivity carriers; in all cases, saturation was reached below 0.2 T. As previously mentioned, this is consistent with petrographic examination of thin sections throughout the massif that reveals the widespread occurrence of opaques, probably magnetite (Fig. 4). Back-field experiments to estimate the remanent coercivity (Hcr) together with (para-magnetism corrected) Hc, Mr, and Ms values from hysteresis (MVSM) show pseudo-single-domain averaged out sizes for the magnetite grains from a variety of samples covering the entire susceptibility range. Interestingly, in Day et al. (1977) diagram, the gabbro and syenite facies (showing much higher bulk susceptibility) are closer to the multi-domain (MD) state than the granitic ones, closer to the single domain one (SD) (Fig. 11c).

The slope of the hysteresis curves after saturation at high fields (fitted between 0.6 and 1 T) represents the para-magnetic (K_p) contribution alone. The ferro-magnetic (S.l.) contribution to susceptibility, $K_f = K - K_p$ (K being the bulk susceptibility), indicates the importance of magnetite in the rock as the main susceptibility carrier. Site S40 shows moderate-to-high values of K_f (48.6%), while sites S16 and S36 show an almost exclusive contribution of K_f (98.3 and 99.3%, respectively). Therefore, caution must be taken in the interpretation of the scalar parameters of the AMS tensor (i.e., T and P').

Since both ferro-magnetic and para-magnetic contributions are present, the bulk susceptibility cannot be used as a measure of the iron content. However, and in spite of the above-mentioned drawbacks, a clear bimodal pattern of K seems to be related to the petrological classification; the gabbro–syenites display higher susceptibility than the granites and the contours of K roughly coinciding with the lithological boundaries (Fig. 12). The highest values appear to the south of the gabbro–syenites, closely associated with the mafic rocks. Susceptibility decreases northwards except for a small increase associated with the westernmost cape of the massif. The granite displays much lower K values, showing maximum records, up to $\sim 12 \times 10^{-3}$ S.I., in the centre of the SIC close to the gabbro–syenite and a strong decreasing trend eastward. In both bodies, the observed susceptibility gradients are sharper than in other non-magnetic granites (Gleizes et al. 1993; Leblanc et al. 1994) that display also much smaller ranges of variability of K.

Magnetic fabrics

A good correlation in orientation can be expected between the shape and the magnetic fabric tensor for isolated magnetite grains (Grégoire et al. 1998). However, the shape anisotropy effect of magnetite aggregates may weaken this correlation, due to the interactions between grains. The alignment of magnetite clusters along the boundaries of other minerals

Table 1 Anisotropy of magnetic susceptibility data of the Sintra massif

Zone	Site	Lat	Log	n	N	ρ (kg/m^3)	K (10^{-6} S.I.)	eK (10^{-6} S.I.)	P'	eP'	T	eT	E_{12}	E_{23}	E_{31}	Dec-K_1	Inc-K_1	*	E_1–K_1	β–K_1	Site	Dec-K_3	Inc-K_3	*	E_1–K_3	β–K_3
B	S-01	38.755577	−9.452911	7	7	2550	11,881	128	1.036	1.004	0.352	0.112	13	5	4	187	44		8270	19.8	S-01	7	48		9771	6.41
B	S-02	38.756646	−9.451066	9	9	2770	68,747	213	1.026	1.007	0.188	0.103	16	9	4	248	40		6516	34.8	S-02	38	46	*	5275	47.4
C	S-04	38.758072	−9.474391	10	10	2500	295	1384	1.016	1.002	0.39	0.112	31	13	8	305	28	e_{12}	6091	38.5	S-04	51	36		8924	14.1
C	S-05	38.752157	−9.463671	8	8	2540	3326	375	1.01	1.002	0.087	0.066	25	20	10	101	44	*	6206	37.5	S-05	201	15	$P <$	7931	23.2
A	S-06	38.762884	−9.406933	7	8	2550	2859	4012	1.059	1.002	0.215	0.162	10	4	2	90	17		9419	9.95	S-06	350	32		9520	8.7
A	S-07	38.756023	−9.429351	7	8	2550	1821	34	1.044	1.002	0.17	0.156	11	7	4	142	24		7080	30	S-07	44	8	*	5450	45.8
C	S-08	38.757300	−9.444153	9	9	2550	4963	953	1.056	1.001	0.05	0.151	9	7	2	221	29	*	5731	41.6	S-08	342	34	*	6359	37.5
C	S-09	38.762187	−9.438034	8	9	2510	8896	160	1.022	1.004	0.036	0.254	15	17	6	56	2		7510	26.3	S-09	329	67		7562	26.5
C	S-10	38.771743	−9.437517	9	9	2570	11,199	65	1.033	1.002	0.364	0.119	12	6	4	173	9		9214	11.7	S-10	286	70		9739	6.71
C	S-11	38.779866	−9.439110	9	9	2530	12,779	260	1.05	1.001	−0.099	0.165	12	13	3	17	14		9432	9.84	S-11	253	72	*	6380	37.3
C	S-12	38.783627	−9.441232	7	8	2520	2199	133	1.021	1.006	−0.018	0.096	15	17	6	28	28		8302	19.5	S-12	273	47	*	6524	36
B	S-13	38.768817	−9.460205	8	8	2680	34,704	2065	1.053	1.005	0.694	0.052	22	3	3	75	47		8202	20.4	S-13	174	8		9895	5.28
A	S-14	38.762917	−9.424175	8	8	2520	4858	2	1.015	1.002	0.255	0.224	25	16	8	257	9		6928	31.3	S-14	8	69		8780	15.4
A	S-15	38.765210	−9.414112	8	8	2500	584	1415	1.013	1.002	0.34	0.15	35	20	12	146	16	e_{12}	6254	37.1	S-15	17	67	$P <$	9893	5.3
A	S-16	38.769404	−9.420272	8	8	2530	2309	59	1.013	1.001	0.043	0.241	33	30	15	138	36	e_{12}	8013	22	S-16	35	31	e_{23}	6871	32.8
A	S-17	38.777395	−9.420523	8	8	2530	419	16	1.014	1.001	0.063	0.065	18	14	7	349	18		8832	15	S-17	166	72		8217	20.6
A	S-18	38.776692	−9.409870	6	7	2570	2196	71	1.034	1.002	0.146	0.162	9	7	4	196	58		8882	14.6	S-18	333	22		8493	18.1
A	S-19	38.787491	−9.398431	9	9	2560	310	1404	1.009	1.002	0.271	0.073	37	23	13	208	35	e_{12}	7246	28.6	S-19	85	36	*	6568	35.6
A	S-20	38.782200	−9.391598	9	9	2560	440	1178	1.012	1.004	−0.243	0.181	21	37	12	270	19	$P <$	6536	34.7	S-20	147	66	e_{23}	5262	47.5
A	S-21	38.785845	−9.386683	9	9	2560	2729	1065	1.044	1.012	0.154	0.182	9	7	3	45	3		8654	16.5	S-21	304	84		7515	27
A	S-22	38.782152	−9.399868	9	9	2560	733	282	1.021	1.003	−0.083	0.145	15	15	6	221	39		8294	19.6	S-22	320	13		8310	19.7
A	S-23	38.790182	−9.386312	7	7	2560	1773	239	1.049	1.003	0.299	0.124	9	4	3	27	9		8482	18	S-23	191	81		8806	15.2
A	S-25	38.780799	−9.387176	6	8	2560	2615	321	1.025	1.004	−0.088	0.096	11	12	5	56	58		9105	12.6	S-25	320	8		8145	21.2
A	S-26	38.773909	−9.389345	7	8	2540	754	966	1.024	1.014	−0.08	0.207	21	27	10	61	18	$P <$	7657	25.1	S-26	332	28	e_{23}	5286	47.3
A	S-27	38.769601	−9.397858	9	9	2580	885	45	1.027	1.004	0.041	0.128	14	10	5	28	29		8807	15.2	S-27	137	31		8005	22.5
A	S-28	38.795017	−9.401193	8	8	2580	2573	2542	1.022	1.006	0.432	0.117	22	9	6	237	13	*	6416	35.7	S-28	146	6		9076	12.7
A	S-29	38.789866	−9.413313	5	6	2570	822	1290	1.013	1.004	−0.262	0.071	22	42	13	216	16	*	5524	43.4	S-29	48	49	e_{23}	5634	44.1
A	S-30	38.786769	−9.410263	9	9	2570	3413	42	1.065	1.001	0.537	0.133	11	3	2	301	46	*	5118	46.8	S-30	134	38		9647	7.54
A	S-31	38.783722	−9.413968	9	9	2550	583	904	1.012	1.002	−0.231	0.152	17	26	9	292	37	*	5459	43.9	S-31	190	9	e_{23}	5986	40.9
C	S-32	38.790687	−9.452869	5	5	2510	470	384	1.018	1.002	0.658	0.106	42	8	7	163	13	e_{12}	4537	51.8	S-32	218	41	*	5904	41.6
A	S-33	38.793716	−9.431165	7	7	2520	1291	1092	1.021	1.004	0.156	0.078	23	20	8	59	14	*	6252	37.1	S-33	180	53		8491	18.1
A	S-34	38.784104	−9.420715	8	8	2580	4546	294	1.033	1.004	0.203	0.138	14	9	5	265	14	*	5624	42.5	S-34	141	46		9064	12.9
A	S-35	38.787259	−9.429039	6	6	2560	2619	923	1.056	1.002	0.001	0.165	6	5	3	39	22	*	6210	37.5	S-35	177	54		8280	20
B	S-36	38.761373	−9.465381	8	8	2760	80,356	1358	1.096	1.005	0.538	0.087	11	2	2	113	8	*	6386	36	S-36	20	13		8494	18.1
C	S-37	38.763355	−9.475424	9	9	2500	1708	526	1.013	1.001	0.311	0.153	27	15	9	151	15	e_{12}	8588	17.1	S-37	49	35		8678	16.4
B	S-38	38.774809	−9.472629	6	6	2360	283	34	1.02	1.002	0.249	0.167	13	9	4	192	41		9754	7.08	S-38	287	7		9903	5.21
C	S-39	38.775825	−9.491219	7	7	2540	9721	85	1.023	1.003	0.393	0.148	24	8	6	158	20		7480	26.6	S-39	54	38		9325	10.5
C	S-40	38.770375	−9.490717	8	8	2460	36	73	1.02	1.004	−0.091	0.16	35	39	17	210	56	e_{12}	6760	32.8	S-40	50	39	e_{23}	9416	9.65
B	S-41	38.780541	−9.483395	7	7	2580	23,259	1041	1.045	1.002	0.72	0.049	29	3	3	290	60	e_{12}	5929	39.9	S-41	102	30		9921	5.05

Table 1 (continued)

Zone	Site	Lat	Log	*n*	*N*	ρ (kg/m^3)	K (10^{-6} S.I.)	eK (10^{-6} S.I.)	P'	eP'	T	eT	E_{12}	E_{23}	E_{31}	Dec-K_1	Inc-K_1	*	E_1–K_1	β–K_1	Site	Dec-K_3	Inc-K_3	*	E_1–K_3	β–K_3
B	S-42	38.781748	−9.495939	9	9	2520	4443	349	1.014	1.005	0.434	0.061	28	10	6	269	63	e_{12}	8241	20.1	S-42	69	24		9153	12
B	S-43	38.790528	−9.491072	8	8	2540	540	437	1.011	1.001	0.034	0.059	30	28	14	290	8	e_{12}	6737	33	S-43	187	36	e_{23}	8389	19
B	S-44	38.785474	−9.480331	6	6	2520	7118	275	1.02	1.002	0.643	0.099	40	6	5	26	4	e_{12}	6959	31	S-44	119	45		9920	5.06
B	S-45	38.787748	−9.479574	8	8	2520	7510	524	1.012	1.002	−0.117	0.205	16	25	9	26	24		8649	16.6	S-45	127	23		8853	14.8
B	S-46	38.771054	−9.446857	6	6	2570	32,367	176	1.018	1.007	0.257	0.185	14	7	5	236	60		7972	22.4	S-46	134	8		9310	10.6
B	S-47	38.777333	−9.446236	4	4	2620	6300	312	1.046	1.015	0.168	0.196	10	5	3	149	4		6840	32.1	S-47	237	43		8301	19.8
B	S-48	38.771479	−9.456225	6	6	2550	13,088	468	1.04	1.003	0.627	0.193	21	4	4	235	13		8650	16.5	S-48	331	28		9897	5.27
B	S-49	38.765594	−9.450163	8	8	2490	8460	138	1.01	1.002	−0.064	0.161	18	21	9	209	62	*P* <	9371	10.4	S-49	346	21	*P* <	8262	20.2
A	S-50	38.7934355	−9.443285	4	4	2500	96	174	1.022	1.003	0.571	0.198	33	7	6	325	18	e_{12}	6307	36.6	S-50	161	62		8806	15.2
B	S-51	38.774909	−9.479679	8	8	2530	2695	64	1.023	1.003	−0.016	0.159	15	12	5	169	34	*	5417	44.3	S-51	27	49	*	6108	39.8
B	S-52	38.784836	−9.467692	9	9	2590	15,850	332	1.039	1.003	0.602	0.174	21	4	3	21	26		9154	12.2	S-52	191	64		9969	4.61
B	S-53	38.780830	−9.464914	6	6	2500	7928	47	1.019	1.002	−0.125	0.116	11	13	6	180	29		7097	29.9	S-53	77	21		9762	6.5
B	S-54	38.780583	−9.458189	8	8	2550	7683	162	1.032	1.005	0.681	0.147	22	4	3	29	1		8292	19.6	S-54	299	29		9489	8.98
B	S-55	38.790353	−9.458459	5	5	2530	3125	1277	1.012	1.001	−0.265	0.111	15	33	9	358	9		9016	13.4	S-55	254	63	e_{23}	7222	29.6
B	S-56	38.799469	−9.477242	3	3	2510	612	13	1.014	1.005	0.068	0.152	25	20	12	0	52	*P* <	7558	25.9	S-56	193	39	*P* <	9710	6.97

#, Site number; *Long & Lat* Longitude and latitude in geographic coordinates, *Zone: A* granite, *B* gabbro–syenite, *C* contact zone, *n/N* number of considered/analyzed specimens, ρ density, *K (eK)* Bulk susceptibility at room temperature and low field (standard error). *P' (eP'), T (eT)* Fabric parameters (Jelinek 1981); Corrected anisotropy degree and shape with their respective standard errors, *E12 (eE12), E23 (eE23), E31 (eE31)* Jelinek (1981) confidence angles and their respective standard errors. K_{max} *mean information. k1-dec, k1-inc* Bingham (1974) mean eigenvector, *K1–E1* Mean Eigenvalues. *ß* tan-1 (E1/E2), K_{min} *mean information: k3-dec, k3-inc* Bingham (1974) mean eigenvector, *K3–E1* mean eigenvalues

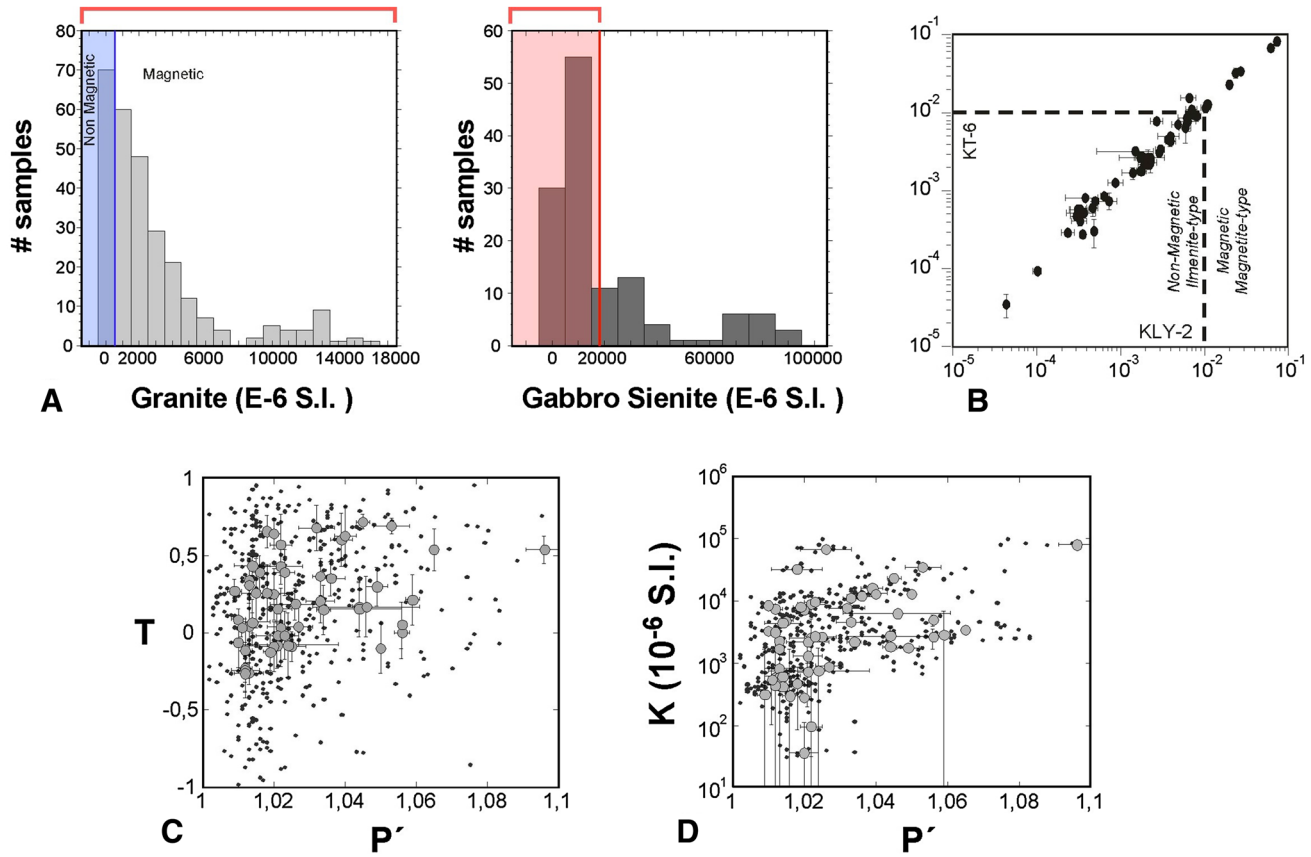

Fig. 10 Bulk susceptibility frequency distribution in the SIC (**a**). The granitic and gabbroic facies are considered separately. All individual measurements (specimens) are used to construct these plots. It is worth noticing that only a small group of samples falls within the "non-magnetic" field, while the main group displays very high susceptibility values (especially the gabbro and syenite facies). **b** Correlation between bulk susceptibility derived from the KLY-2 and the KT-6 (field) susceptometer. **c** Relationship between anisotropy degree (P') and shape parameter (T). **d** Relationship between anisotropy degree (P') and bulk susceptibility value (K). In these two latter plots, individual measurements (black dots) were plotted together with site-means (and error bars)

usually results in a magnetic fabric similar to that caused by biotites, but with a larger scatter of the principal susceptibility axes (Archanjo et al. 1995). In the SIC, directional data should be considered with caution due to the occurrence of pseudo-single and multi-domain magnetites. The correlation between the bulk susceptibility (K) and the anisotropy degree (P'; Fig. 10e) may be used as an indicator of magnetite-controlled fabric with the subsequent addition of noise (directional data) and reduction of reliability of the AMS parameters.

In addition to the complexity of its magnetic mineralogy, the SIC mostly shows triaxial–oblate fabrics (Fig. 10d). Therefore, the magnetic lineations were processed with especial care. Quality criteria established for AMS directional data (Pueyo et al. 2004) suggest that our interpretation should be only based on reliable data (see Fig. 13: in black); the remaining set should be considered with more caution (see Fig. 13: in gray).

To double-check the relationships between the magnetic fabric and the mineral fabric, image analysis in different petrographic facies was performed. Three thin sections were cut perpendicular to the minimum magnetic axis K_3 in gabbro, syenite, and granite samples (Fig. 14). For the image analysis, we used the INTERCEPT program of Launeau and Robin (1996). In the gabbro facies (Fig. 14a), the mineral fabric is defined mainly by the alignment of euhedral plagioclases, while in the granite, both feldspars and quartz define the mineral fabric (Fig. 14b). The syenite (Fig. 14c) shows a complex fabric with a primary, very well-defined magmatic fabric modified by a cross-cutting secondary fabric marked by cataclasis of plagioclases along shear bands. Image analysis of this section shows the maximum axis of the image analysis equivalent ellipse parallel to the K_2 axis of the magnetic ellipsoid. Therefore, in two of the three analyzed examples, a good correlation between the magnetic and the mineral preferred orientation can be inferred. In the analyzed syenite sample, cataclasis precludes a direct interpretation of the magnetic fabric, and K_1–K_2 magnetic axes are switched with respect to the mineral fabric orientations inferred from thin sections.

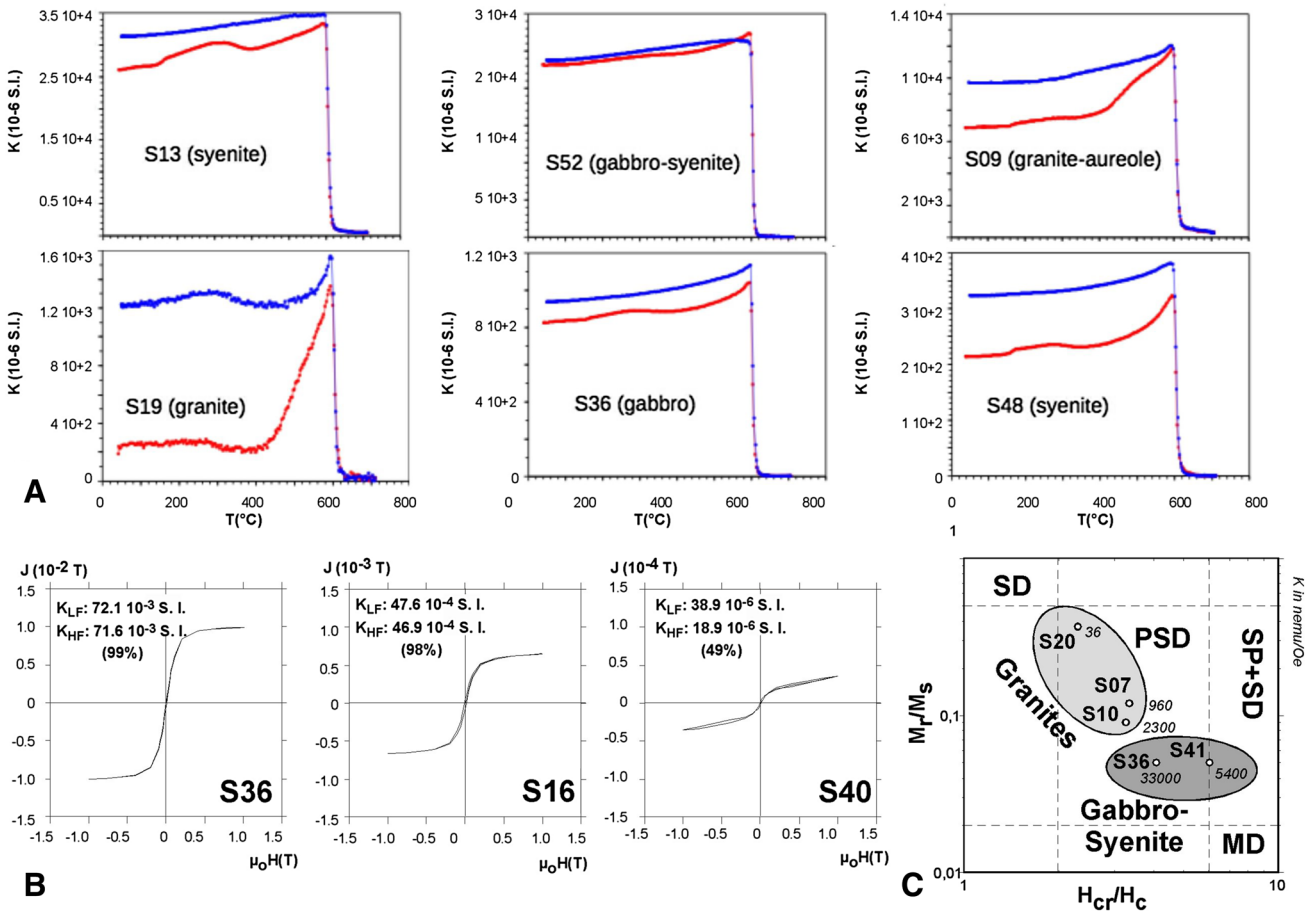

Fig. 11 Rock magnetism analyses in the SIC. **a** Susceptibility-temperature (*k–T*) curves for the three main lithological types found in the SIC: granites within and far from the aureole surrounding the gabbro–syenitic body, syenite, and gabbro (curves e, f). Note that the bulk susceptibility (not normalized in the diagrams) is strongly dependent on the magnetite content of the rock, regardless of the petrographic facies. See text for further explanation. **b** Hysteresis loops in three representative samples (para-magnetic slopes have been corrected). **c** Day's et al. (1970) diagram displaying the grain-size distribution of magnetite

In cases where late brittle deformation overprints the magmatic fabric, especially when the anisotropy degree is low, magnetic fabric must be carefully interpreted to reconcile these fabrics with geological events.

The inspection of the magnetic lineations map shows that there is no clear overall trend within the SIC (Fig. 13b, Appendix 1). If the gabbro–syenite and granite bodies are observed separately, clearer patterns are depicted. The granite unit systematically displays shallowly plunging (< 30°) lineations. NE–SW trends dominate in the easternmost part of the massif, but these values tend to point to the north, more-or-less parallel to the petrological contact, in the vicinity of the gabbro–syenite (Fig. 13a). The gabbro–syenite body presents a different lineation distribution, mostly N–S in trends and much steeper in plunges (Fig. 13b). A several km-wide aureole where the orientation of magnetic lineation is more similar to the gabbro–syenite facies than to the rest of the granite can be distinguished (Fig. 13), and consequently, a separate stereoplot for these sites is shown.

The magnetic foliations in the granite show a general E–W strike (Fig. 13c) except at the borders where they tend to parallel the contact with the country rocks. In the central part of the granite, a WSW–ENE trending divide can be outlined: i.e., in the north of the massif, the foliations dip to the north, whereas in the southern sector, they dip to the south. Foliations within the gabbro–syenite are steeper and their poles distribute within a girdle whose pole is the magnetic lineation.

Interpretation and discussion

Geometry of the SIC

The present gravimetric study confirms that the SIC is made of two types of intrusive bodies with sharply different

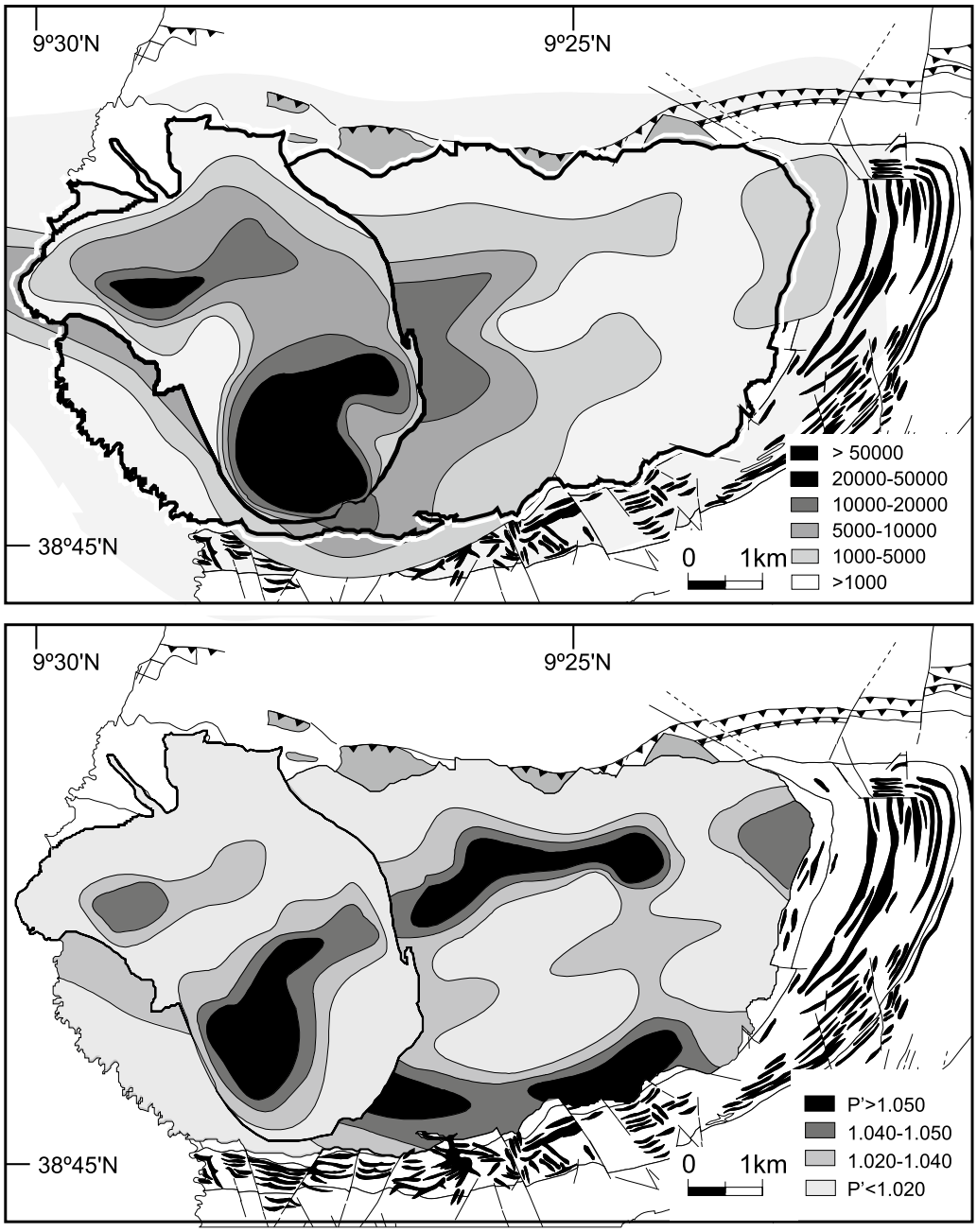

Fig. 12 Contour maps of spatial distribution of magnetic susceptibility in the SIC: **a** bulk magnetic susceptibility (Kmean), and **b** corrected magnetic anisotropy degree (*P′* of Jelinek 1981)

geometries (plugs and laccoliths) and densities (gabbro and diorite versus granite and syenite, in spite that, as previously stated, the syenite is genetically related to the gabbro body). According to the modeled cross sections (Fig. 7), the preserved thickness of the granitic body is 500 m in average. The syenitic body also shows a sheet-like shape, with an average thickness of 1000 m (section 2–2′, Fig. 7), but its reliable reconstruction is more difficult because of its relationship with the gabbro. Some of the gravity lows within the low-density body can be explained by a greater thickness (root zones) of the syenitic sheet (see, for example, cross section 1–1′, Fig. 7). Other negative anomalies, especially in the northern border of the massif, can be explained by (i) the lower density of the Cretaceous and Eocene–Oligocene series with respect to the Jurassic series, with a combined thickness of about 1000 m in the core of the syncline

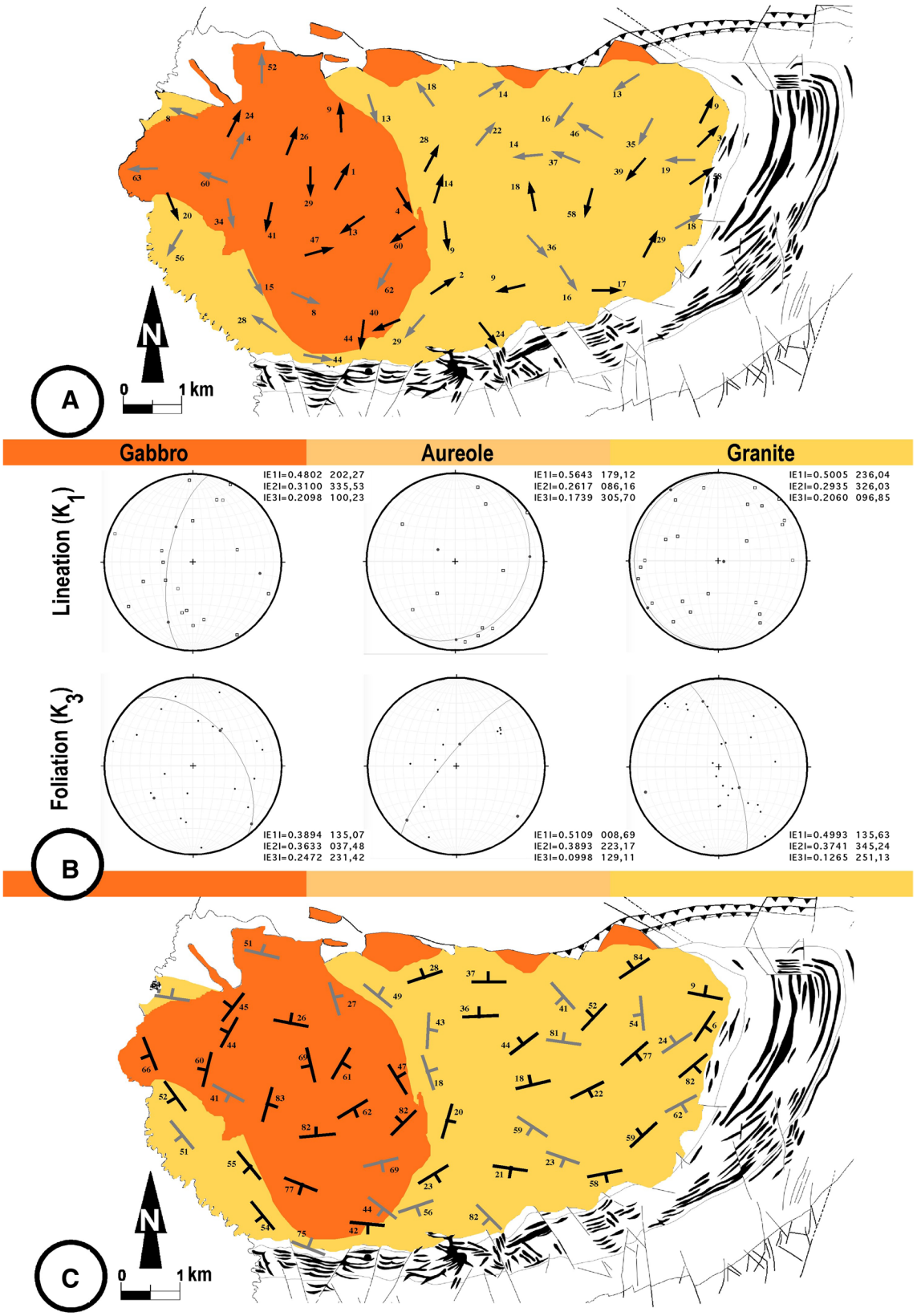

Fig. 13 Magnetic fabric in the Sintra Igneous complex (equal area, lower hemisphere projections, and calculated eigenvalues): **a** magnetic lineations; **b** lineation and foliation stereoplots for the gabbro–syenite, granite, and granite aureole, and **c** foliations map obtained from the AMS study. Black and gray colors indicate first- and second-class directional data, respectively

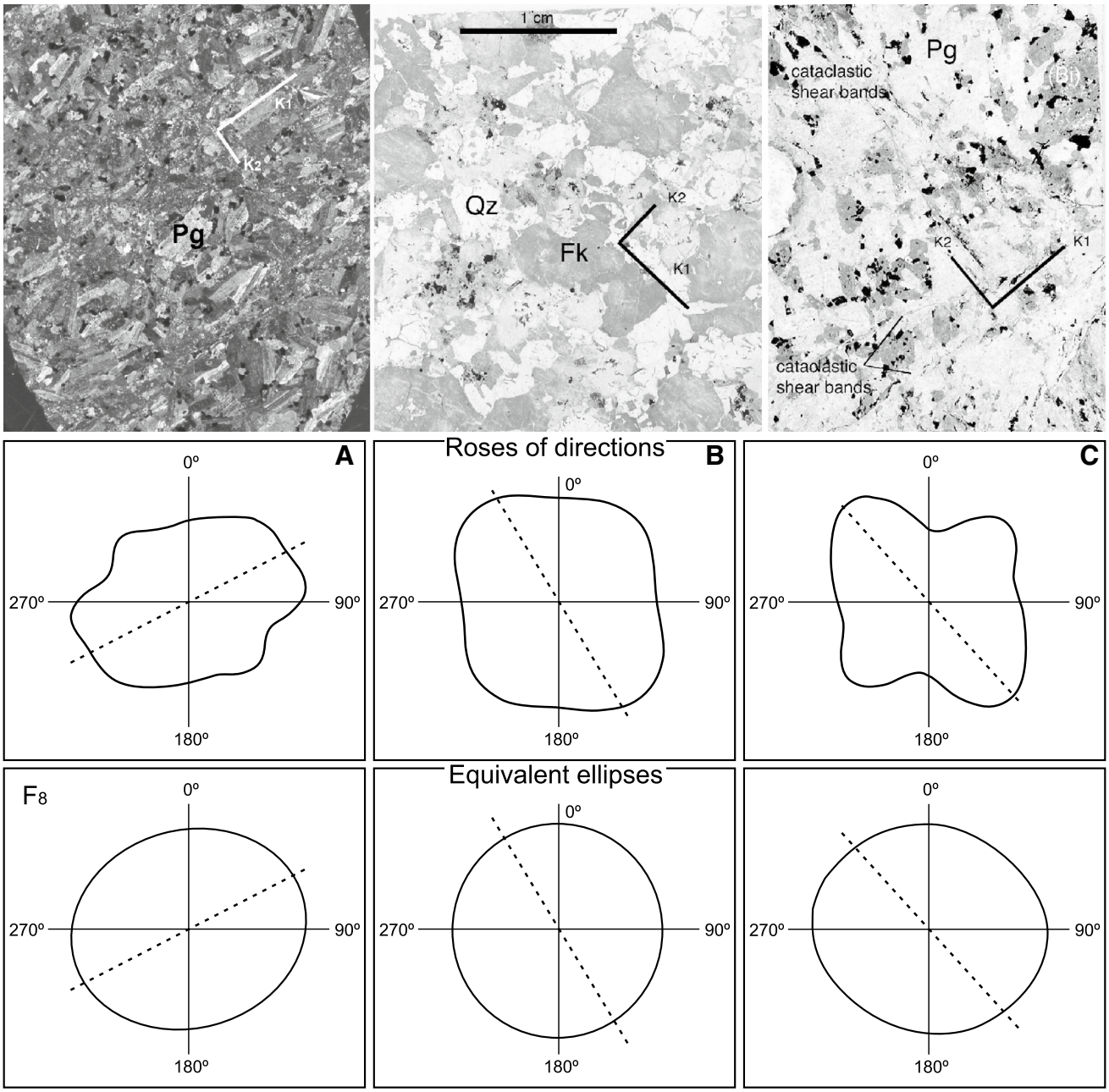

Fig. 14 Image analysis by means of the INTERCEPT program (Launeau and Robin 1996) of three sections including: **a** gabbroic facies (site S-36, crossed polarizers); **b** granite (site S-5, parallel polarizers), and **c** gabbro–dioritic facies with cataclastic shear bands (site S-36, parallel nichols). *Pg* plagioclase, *Fk* K-feldspar, *Bi* biotite, *Qz* quartz. The orientations of the magnetic fabrics axes contained in the plane of the section are noted $K_1 > K_2$. The rose of directions and equivalent shape ellipse are shown for each section. See text for explanation

located near the Sintra thrust, and (ii) the existence of syenite or granite in the footwall of the Sintra thrust, allowing us to interpret a post-emplacement reverse fault consistent with its geological history. All in all, the laccolith geometry of the granite–syenite body can be assessed from the geometry of its floor inferred from the gravimetric models and from the strong uplift of the beds sealing the top of the intrusion that can be reconstructed from dip of beds and the cross section (see Figs. 3b, 5), which cannot be explained only by tilting due to the Cenozoic compression. Positive anomalies beyond the contact between the SIC and the country rock can be explained by the higher density of basic sills and dykes (cross section 4–4′, Fig. 7) emplaced within the Jurassic and the Cretaceous rocks.

The strongest positive gravity anomaly in the southwest of the SIC coincides with the outcrop of the gabbroic facies

that surrounds the syenite. This positive anomaly is local and changes abruptly to the north to a negative anomaly that can be explained by the presence of a syenitic sheet extending to a maximum depth of 1200 m below sea level (Fig. 8). According to gravity modeling, the gabbroic body should have a maximum width of 1.5 km and hence should reach depths of several kilometers in some sections (Fig. 8), consistent with the strong magnetic anomaly associated with the SIC (Silva et al. 2000). From this central zone, the roots of this gabbroic body appear to branch toward the northeast and the southeast. These two directions are parallel to the main regional faults (see Figs. 2, 3) and the orientation of the central, main outcrop of gabbro–syenite.

The gravity anomalies reveal that the roots of the mafic bodies appear in three areas, one of which coincides with the main gabbro–syenite outcrop in the central part of the southern limit of the SIC. The other two are interpreted as plugs that are topped by the younger granite laccolith. The NE–SW trending branch of the positive gravity anomalies coincides with the main fracture system within the granite, which was re-activated with left-lateral strike-slip movement during the Cenozoic tectonic inversion events. The NW–SE direction coincides with the outcrop direction of the main gabbro–syenite body and is parallel to the NW–SE trending Roca-Espichel Fault Zone (see Fig. 2) that hosts numerous

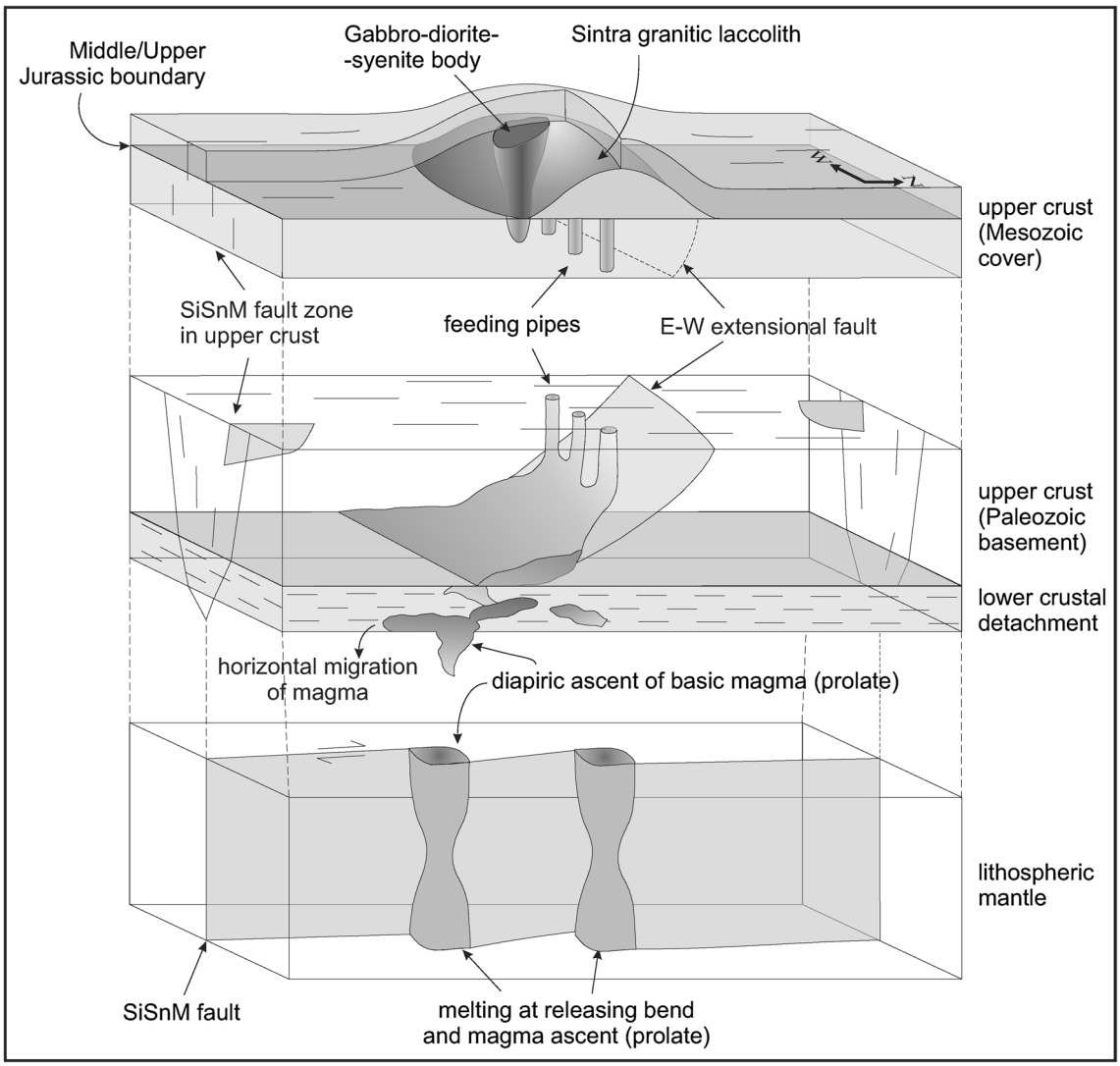

Fig. 15 Schematic block diagram synthesizing the proposed mode of extraction, ascent, and emplacement of the SIC. Extraction occurred from the sub-lithospheric mantle (according to isotopic data by Grange et al. 2010) by means of decompression at extensional jogs of the NNW–SSE trending Sintra–Sines–Monchique fault. The granitic magma ascended along the fault and formed an elongated E–W laccolith under an approximate N–S compressive field. The later gabbro–syenite magma also ascended along the same fault. At crustal level, both magmas were injected along rift-inherited faults with E–W and NE–SW strikes

vertical dykes, as well as to the offshore west boundary of the Estremadura Spur (Neves et al. 2009).

AMS directional data and flow directions

Concerning the AMS data, the gabbro–syenite displays a concentric distribution of foliations and the lineations define a steeply dipping, NNE–SSW trending great circle (Fig. 13). The granite surrounding the gabbro–syenite intrusion (aureole) displays foliations parallel to the contact, whilst the lineation plunges are shallower than in the gabbro–syenite. The remaining foliation planes in the granite depict an NNW–SSE trending great circle, whose pole coincides with the magnetic lineation concentration maximum. According to the cited geochronological dating (Miranda et al. 2009; Grange et al. 2010), the granite is slightly younger than the gabbro, and therefore, a plausible mechanism to explain this fabric development could consider the accommodation of the granite magma flowing around an already existing, rigid body (gabbro) with considerably higher melting point. This would explain the orientation of magnetic fabrics in the aureole of granite surrounding the gabbro–syenite body.

It is worth comparing the gravity anomaly contour map and the AMS foliation/lineation distribution; there is a scatter of the lineation/foliation orientations where the granite overlies the north-eastern positive gravity anomaly. This suggests that the buried gabbro plug, i.e., a vertical magma conduit, was probably re-used for the ascent of the granitic magma, originating a non-planar, local AMS fabric.

Emplacement model

After gathering all the geological and geophysical information presented in this paper (field observations, gravimetry, and AMS) and petrological and radiometric dating, the following sequence of magmatic events is proposed for the origin of the SIC: (i) intrusion of the basic sills presently surrounding the SIC; (ii) intrusion of the gabbro–diorite–syenite bodies using the previous anisotropies (roots); (iii) intrusion of the granite magma that formed the laccolith, uplifting the cover and stretching the Jurassic and Cretaceous host rocks as well as the basic sills; (iv) intrusion of the cone-sheets, and (v) intrusion of the radial dykes.

The ENE–WSW trending magnetic lineation is perpendicular to the NNW–SSE trending lineament defined by Roca-Espichel fault zone and the Sintra–Sines–Monchique intrusions (Figs. 1, 2). This observation suggests intrusion of the granite magma mainly along the NNW–SSE sub-vertical fault, spreading parallel to the ENE–WSW direction along a stratigraphic unconformity, either exclusively controlled by magma flow (see, e.g., Paterson et al. 1998) or perpendicular to the direction of the main compression direction in Campanian times (~ 80 Ma, age of the granite). Similar results (ENE–WSW trending lineations) were found also in the Monchique syenite (~ 72 Ma) by means of AMS analysis (Barbosa 1999).

Although there is no strong local field evidence for compression at this age due to the lack of post-Cenomanian through Paleogene sediments, it has been shown that the southern Portuguese Margin was shortened as a result of approximately N–S oriented compression during the Late Cretaceous (Terrinha 1998; Lopes et al. 2006; Ramos et al. 2015). Palinspastic reconstructions indicate an approximate N–S movement of Africa with respect to Eurasia during the Late Cretaceous after the counter-clockwise rotation of the Iberian plate (Dewey et al. 1989; Schettino and Scotese 2002). Similar modes of emplacement under a strong control of a deep-seated fault parallel to the shortening compression have been reported for the late-Variscan granites (Román-Berdiel et al. 1995a, b; Aranguren et al. 2003) in NW Iberia.

It is here proposed that the Sintra–Sines–Monchique lineament corresponds to a deep-seated fault that broke through the upper crust only at the rifted margins of the Lusitanian and Algarve Basins, i.e., it is not present in the areas of the Sines and Monchique intrusions that were emplaced into non-rifted basement (see Fig. 1). This fault favored the ascent of magma from the lithospheric mantle (according to the chemical/isotopic composition of the magmatic suite, Grange et al. 2010) up to a detachment located somewhere below the upper crust, possibly by means of adiabatic decompression at releasing bends (in the sense of Sylvester 1988, Fig. 15). The magma would then intrude through the uppermost crust along E–W trending faults in the case of Sines and Monchique intrusions that were active as extensional/transfer faults during the Jurassic through Early Cretaceous rifting. In the case of the SIC, the Sintra–Sines–Monchique fault reached the uppermost crust (Roca-Espichel fault zone, Fig. 2) accommodating the ascent and emplacement of these magmas, as shown by the NNW–SSE shape of the gabbro–syenite intrusion.

Conclusions

The geometry of the SIC can be characterized as a composite intrusion consisting of a granite laccolith (~ 80 Ma), elongated E–W topping vertical gabbroic plugs and syenite plug and laccolith (~ 90 Ma). A complex of sills and dykes are included in the SIC, being the basic sills precursor of the gabbro intrusives; the ring felsic dykes, and radial dykes post-date the granite.

In spite of comprising both magnetite- and ilmenite-series igneous bodies (the range of bulk susceptibility exceeds four orders of magnitude), the SIC provides consistent AMS

directional results in agreement with independent preferred orientation analysis. This confirms that AMS is a useful tool to characterize magnetic (magmatic) fabric in both types of rocks.

The internal, magmatic structures within the massif display (i) steeply plunging lineations and concentric foliations in the plugs, probably linked to magma ascent, and (ii) shallow plunging lineations associated with shallow-dipping foliations in the granite laccolith. Lineations within the laccolith show a dominant ENE–WSW orientation approximately parallel to the body elongation.

The intrusion of the two magmatic bodies (granite and gabbro–syenite) can be ascribed to two sequential alkaline magmatic episodes in the passive Iberian margin. The location of the feeding planes and pipes during both episodes was controlled by pre-existing faults of NNW–SSE, E–W, and NE–SE orientation, probably Late-Variscan faults that were active during the Jurassic-Early Cretaceous rifting of the West Iberia Margin.

Acknowledgements Rock magnetism analyses were partially done in the ICMA laboratory (Univ. of Zaragoza) with the help of C. Rillo and J. Sesé to whom we are very grateful. The authors are also very grateful to Philip Tomek, Marlina Elburg, and an anonymous referee for their helpful comments.

Appendix 1

Equal-area, lower hemisphere projection of magnetic fabrics of individual samples grouped by sites in the Sintra Massif (granite, gabbro, and syenite, see location of sites in Fig. 9). k_1: hollow squares, k_3: black circles. Axes of Bingham distribution for each site are also indicated.

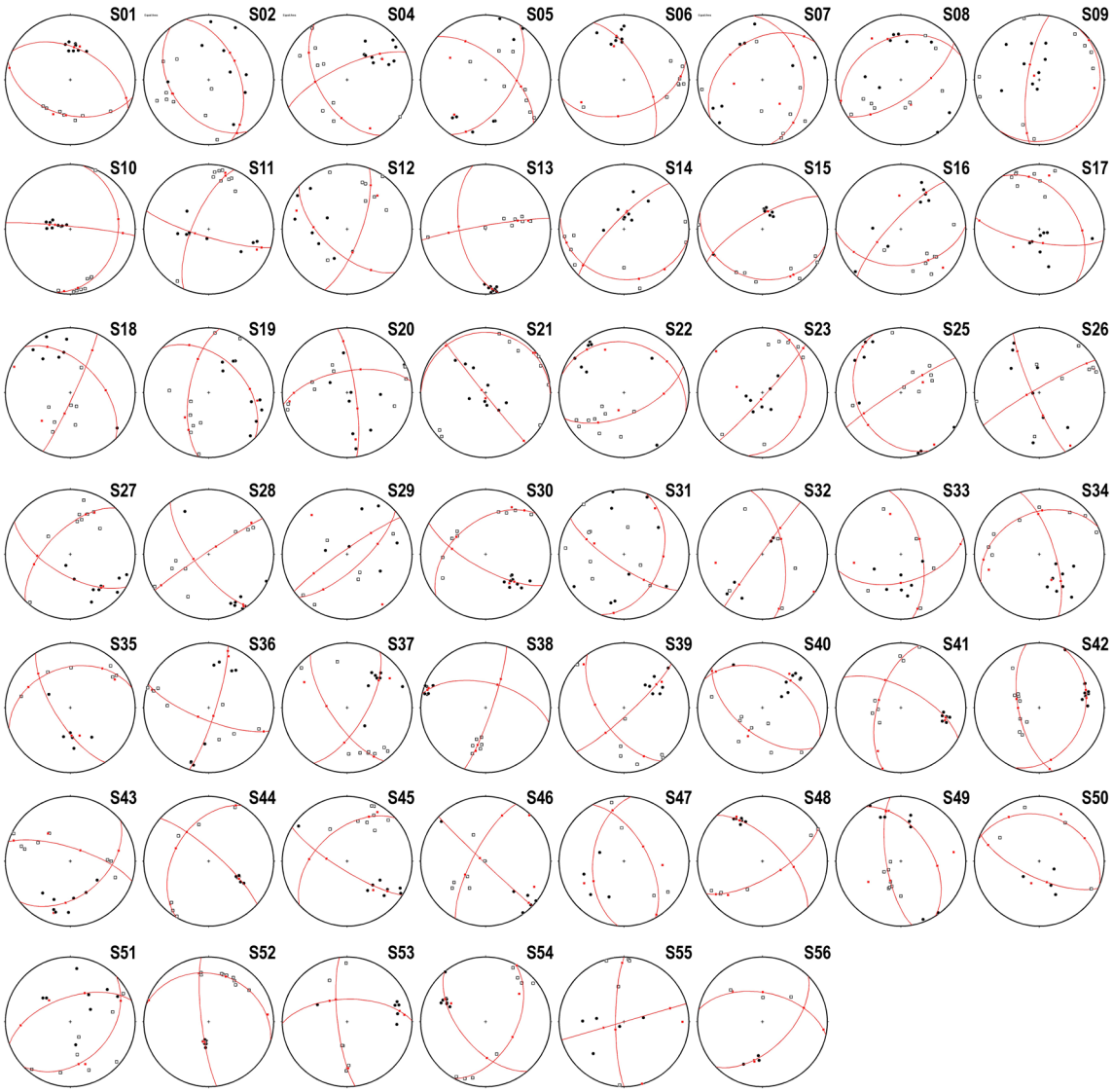

References

Alves MCA (1964) Estudo Petrológico do Maciço de Sintra. Revista da Faculdade de Ciências de Lisboa, 2ª série, C, 12(2):123–289

Alves TM, Moita C, Sandnes F, Cunha T, Monteiro JH, Pinheiro LM (2006) Mesozoic–Cenozoic evolution of North Atlantic continental-slope basins: The Peniche basin, western Iberian margin. AAPG Bulletin 90:31–60

Aranguren A, Tubia JM, Bouchez JL, Vigneresse JL (1996) The Guitiriz granite, Variscan belt of northern Spain: extension-controlled emplacement of magma during tectonic escape. Earth Planet Sci Lett 139:165–176

Aranguren A, Cuevas J, Tubia JM, Román Berdiel T, Casas A, Casas-Ponsati A (2003) Granite laccolith emplacement in the Iberian Arc: AMS and gravity study of the La Tojiza pluton (NW Spain). J Geol Soc Lond 160:435–445

Arbaret L, Diot H, Bouchez JL, Launeau P (1995) Tridimensional shape preferred orientation of particles in experimental simple shear flow; AMS fabric and image analysis. J Czech Geol Soc 40:57–58

Archanjo CJ, Launeau P, Bouchez JL (1995) Magnetic fabric vs. magnetite and biotite shape fabrics of the magnetite-bearing granite pluton of Gameleiras (Northeast Brazil). Phys Earth Planet Inter 89:63–75

Barbosa SA (1999) Estudo geoestatístico de dados experimentais da anisotropia da susceptibilidade magnética de rochas do maciço de Monchique (Doctoral dissertation, Universidade do Porto). https://repositorio-aberto.up.pt/bitstream/10216/12443/2/Texto%20integral.pdf. Accessed 2017

Bingham C (1974) An antipodally symmetric distribution on the sphere. Annales Stat 2:1201–1225

Borradaile GJ, Henry B (1997) Tectonic applications of magnetic susceptibility and its anisotropy. Earth Sci Rev 42:49–93

Borradaile GJ, Jackson M (2010) Structural geology, petrofabrics and magnetic fabrics (AMS, AARM, AIRM). J Struct Geol 32:1519–1551

Borradaile GJ, Werner T (1994) Magnetic anisotropy of some phyllosilicates. Tectonophysics 235:223–248

Bouchez JL (1997) Granite is never isotropic: an introduction to AMS studies of granitic rocks. In: Bouchez JL, Hutton DHV, Stephens WE (eds) Granite: from segregation of melt to emplacement fabrics. Dordrecht, The Netherlands, pp 95–112

Bouchez JL (2000) Anisotropie de susceptibilité magnétique et fabrique des granites. Comptes rendus de l'Académie des Sciences 330:1–14

Bouchez JL, Gleizes G, Djouadi T, Rochette P (1990) Microstructure and magnetic susceptibility applied to emplacement kinematics of granites: the example of the Foix pluton (French Pyrenees). Tectonophysics 184:157–171

Bronner A, Sauter D, Manatschal G, Peron-Pinvidic G, Munschy M (2011) Magmatic breakup as an explanation for magnetic anomalies at magma-poor rifted margins. Nat Geosci 4:549–553

Calvín P, Ruiz-Martínez VC, Villalaín JJ, Casas-Sainz AM, Moussaid B (2017) Emplacement and deformation of Mesozoic gabbros of the High Atlas (Morocco): Paleomagnetism and magnetic fabrics. Tectonics 36. https://doi.org/10.1002/2017TC004578

Carvalho AMG (1994) O Cenozóico Continental a norte da Serra de Sintra (estudo tectono-sedimentar). Mem Geociências Univ Lisboa 1:1–89

Day R, Fuller M, Schmidt VA (1977) Hysteresis properties of titanomagnetites: grain size and composition dependence. Phys Earth Planet Inter 13:260–267

Dewey JF, Helman ML, Knott SD, Turco E, Hutton DHW (1989) Kinematics of the western Mediterranean. Geol Soc Lond Spec Publ 45(1):265–283

Ellwood BB, Wenner DB (1981) Correlation of magnetic susceptibility with $^{18}O/^{16}O$ data in late orogenic granites of the southern Appalachian Piedmont. Earth Planet Sci Lett 54:200–202

Gleizes G, Nédélec A, Bouchez JL, Autran A, Rochette P (1993) Magnetic susceptibility of the Mont Louis-Andorra ilmenite-type granite (Pyrenees): a new tool for the petrographic characterization and regional mapping of zoned granite plutons. J Geophys Res 98:4317–4331

Graham JW (1954) Magnetic anisotropy: an unexploited petrofabric element. Geol Soc Am Bull 65:1257–1258

Grange M, Scharer U, Cornen G, Girardeau J (2008) First alkaline magmatism during Iberia-Newfoundland rifting. Terra Nova 20:494–503

Grange M, Scharer U, Merle R, Girardeau J, Cornen G (2010) Plume–lithosphere interaction during migration of cretaceous alkaline magmatism in SW Portugal: evidence from U–Pb ages and Pb–Sr–Hf isotopes. J Petrol 51:1143–1170

Grégoire V, Saint-Blanquat M, Nédélec A, Bouchez JL (1995) Shape anisotropy versus magnetic interactions of magnetite grains; experiments and application to AMS in granitic rocks. Geophys Res Lett 22:2765–2768

Grégoire V, Darrozes J, Gaillot P, Nédélec A, Launeau P (1998) Magnetite grain shape fabric and distribution anisotropy vs. rock magnetic fabric; a three-dimensional case study. J Struct Geol 20:937–944

Ishihara S (1977) The magnetite-series and ilmenite-series granitic rocks. Min Geol 27:293–305

Izquierdo-Llavall E, Román-Berdiel T, Casas AM, Oliva-Urcia B, Gil-Pena I, Soto R, Jabaloy A (2012) Magnetic and structural study of the Eaux-Chaudes intrusion: understanding the Variscan deformation in the Western Axial Zone (Pyrenees). Int J Earth Sci 101(7):1817–1834

Jelinek V (1981) Characterization of the magnetic fabric of rocks. Tectonophysics 79:63–70

Kullberg JC (2000) Evolução tectónica mesozóica da Bacia Lusitaniana, Ph.D. thesis, Universidade Nova de Lisboa, Lisboa

Kullberg MC, Kullberg JC, Terrinha P (2000) Tectónica da Cadeia da Arrábida. In Tectónica das regiões de Sintra e Arrábida, Mem. Geociências Univ Lisboa 2:35–84

Kullberg JC, Rocha RB, Soares AF, Rey J, Terrinha P, Azeredo AC, Callapez P, Duarte LV, Kullberg MC, Martins L, Miranda JR, Alves C, Mata J, Madeira J, Mateus O, Moreira M, Nogueira CR (2013) A Bacia Lusitaniana: Estratigrafia, Paleogeografia e Tectonica. In: Dias R, Araújo A, Terrinha P, Kullberg JC (eds) Geología de Portugal. Geologia Meso-cenozóica de Portugal, vol II. Lisboa Escolar editora, pp 195–347

Launeau P (1990) Analyse numérique des images et orientations préférentielles de forme des agrégats polyphasés: Application à l'analyse cinématique des granites. Ph.D. thesis, Université Paul Sabatier de Toulouse

Launeau P, Robin PY (1996) Fabric analysis using the intercept method. Tectonophysics 267:91–119

Leblanc D, Gleizes G, Lespinasse P, Olivier P, Bouchez JL (1994) The Maladeta granite polydiapir, Spanish Pyrenees: a detailed magneto-structural study. J Struct Geol 16:223–235

Lopes FC, Cunha PP, Le Gall B (2006) Cenozoic seismic stratigraphy and tectonic evolution of the Algarve margin (offshore Portugal, southwestern Iberian Peninsula). Mar Geol 231:1–36

Mahmoudi A (1991) Quelques intrusions alcalines et basiques du Cretacée Supérieur au Portugal (région de Lisbonne). Ph.D. thesis, Université de Nancy I

Martín-Hernández F, Hirt AM (2003) The anisotropy of magnetic susceptibility in biotite, muscovite and chlorite single crystal. Tectonophysics 367:13–28

Martins L (1991) Actividade ígnea Mesozóica em Portugal (Contribuição Petrológica e Geoquímica). Ph.D. thesis, Universidade de Lisboa

Martins L, Madeira J, Youbi N, Munhá J, Mata J, Kerrich R (2008) Rift-related magmatism of the Central Atlantic Magmatic Province in Algarve, Southern Portugal. Lithos 101:102–124

Mata J, Alves CF, Martins L, Miranda R, Madeira J, Pimentel N, Martins S, Azevedo MR, Youbi N, De Min A, Almedida IM, Bensalah MK, Terrinha P (2015) $^{40}Ar/^{39}Ar$ ages and petrogenesis of the West Iberian Margin onshore magmatism at the Jurassic-Cretaceous transition: geodynamic implications and assessment of open-system processes involving saline materials. Lithos 236–237:156–172

Mezcua J, Gil A, Benarroch R (1996) Estudio gravimétrico de la Península Ibérica y Baleares, 2. Ministerio de Fomento, Instituto Geográfico Nacional, Madrid maps

Miranda R, Valadares V, Terrinha P, Mata J, Azevedo MA, Kullberg JC, Ribeiro C (2009) Age constraints on the Late Cretaceous alkaline magmatism on the West Iberia Margin. Cretac Res 30:575–586

Montenat C, Guéry F, Jamet M, Berthou PY (1988) Mesozoic evolution of the Lusitanian basin: comparison with the adjacent margin. In: Boillot G et al (eds) Proceedings of the ocean drilling program, scientific results, vol 103, pp 757–775

Nédelec A, Bouchez JL (2015) Granites: petrology, structure, geological setting and metallogeny. Oxford University Press, Oxford

Neres M, Bouchez JL, Terrinha P, Font E, Moreira M, Miranda R, Launeau P, Carvallo C (2014) Magnetic fabric in a Cretaceous sill (Foz da Fonte, Portugal): flow model and implications for regional magmatism. Geophys J Int 199(1):78–101. https://doi.org/10.1093/gji/ggu250

Neves MC, Terrinha P, Afilhado A, Moulin M, Matias L, Rosas F (2009) Response of a multi-domain continental margin to compression: Study from seismic reflection–refraction and numerical modelling in the Tagus Abyssal Plain. Tectonophysics 468:113–130. j.tecto.2008.05.008

Paterson SR, Fowler TK, Schmidt KL, Yoshinobu AS, Yuan ES, Miller RB (1998) Interpreting magmatic fabric patterns in plutons. Lithos 44(1):53–82

Pearce J (1996) Sources and settings of granitic rocks. Episodes 19:120–125

Pedley RC (1991) GRAVMAG user manual: interactive 2.5D gravity and magnetic modelling program. British Geological Survey, Keyworth

Pignotta GS, Benn K (1999) Magnetic fabric of the Barrington Passage Pluton, Meguma Terrane, Nova Scotia: a two-stage fabric history of syntectonic emplacement. Tectonophysics 307:75–92

Pinheiro LM, Wilson RCL, Reis RP, Whitmarsh RB, Ribeiro A (1996) The Western Iberia Margin: a geophysical and geological overview. In: Whitmarsh RB, Sawyer DS, Klaus A, Masson DG (eds) Proceedings of the ocean drilling program, scientific results, vol 149, pp 3–23

Pueyo EL, Román Berdiel MT, Bouchez JL, Casas AM, Larrasoaña JC (2004) Statistical significance of magnetic fabric data in studies of paramagnetic granites. In: Martín-Hernández F, Luneburg CM, Aubourg C, Jackson M (eds), Magnetic fabric: methods and applications, vol 238. Geological Society of London, Special Publications, London, pp 395–420

Pueyo-Anchuela O, Casas AM, Pueyo EL, Pocoví A, Gil-Imaz A (2013) Analysis of the ferromagnetic contribution to the susceptibility by low field and high field methods in sedimentary rocks of the Southern Pyrenees and Northern Ebro foreland basin (Spain). Terranova 25(4):307–314

Ramos A, Fernández O, Terrinha P, Muñoz JA (2015) Extension and inversion structures in the Tethys-Atlantic linkage zone, Algarve Basin, Portugal. (**IJES-D-15–00219R1**)

Rasmussen ES, Lomholt S, Andersen C, Vejbæk OV (1998) Aspects of the structural evolution of the Lusitanian Basin in Portugal and the shelf and slope area offshore Portugal. Tectonophysics 300:199–225

Ribeiro A, Antunes MT, Ferreira MP, Rocha R, Soares A, Zbyszewski G, Moitinho de Almeida F, Carvalho D, Monteiro JH (1979) Introduction à la géologie générale du Portugal. Serviços Geológicos de Portugal, Lisboa, p. 114

Ribeiro A, Kullberg MC, Kullberg JC, Manuppella G, Phipps S (1990) Review of Alpine tectonics in Portugal. Foreland detachment in basement and cover rocks. Tectonophysics 184:357–366

Rocchi S, Westerman DS, Dini A, Innocenti F, Tonarini S (2002) Two-stage growth of laccoliths at Elba Island, Italy. Geology 30:983–986

Rochette P (1987) Magnetic susceptibility of the rock matrix related to magnetic fabric studies. J Struct Geol 9:1015–1020

Rochette P, Jackson M, Aubourg C (1992) Rock magnetism and the interpretation of anisotropy of magnetic susceptibility. Rev Geophys 30:209–226

Rock NMS (1982) The Late Cretaceous alkaline igneous province in the Iberian Peninsula, and its tectonic significance. Lithos 15:111–131

Román-Berdiel T, Pueyo-Morer EL (2000) Distribution d'orientation des joints et relation avec l'anisotropie magmatique primaire dans le massif granitique de Trives (Nord-Ouest de l'Espagne). Comptes Rendus de l'Académie des Sciences-Series IIA-Earth and Planetary Science 330(6):437–443

Román-Berdiel T, Pueyo-Morer EL, Casas-Sainz AM (1995a) Granite emplacement during contemporary shortening and normal faulting: structural and magnetic study of the Veiga massif (NW Spain). J Struct Geol 17:1689–1706

Roman-Berdiel T, Gapais D, Brun JP (1995b) Analogue models of laccolith formation. J Struct Geol 17:1337–1346

Roman-Berdiel TR, Gapais D, Brun JP (1997) Granite intrusion along strike-slip zones in experiment and nature. Am J Sci 297:651–678

Schettino A, Scotese CR (2002) Global kinematic constraints to the tectonic history of the Mediterranean region and surrounding areas during the Jurassic and Cretaceous. J Virtual Explor 8:149–168

Silva EA, Miranda JM, Luis JF, Galdeano A (2000) Correlation between the Palaeozoic structures from West Iberian and Grand Banks margins using inversion of magnetic anomalies. Tectonophysics 321:57–71

Stapel G (1999) The nature of isostasy in West Iberia (and its bearing on Mesozoic and Cenozoic regional tectonics). Ph.D. thesis, Vrije Universiteit, Amsterdam

Stapel G, Cloetingh S, Pronk B (1996) Quantitative subsidence analysis of the Mesozoic evolution of the Lusitanian basin (western Iberian margin). Tectonophysics 266:493–507

Sylvester AG (1988) Strike-slip faults. Geol Soc Am Bull 100(11):1666–1703

Tarling DH, Hrouda F (1993) The magnetic anisotropy of rocks. Chapman & Hall, London

Terrinha PAG (1998) Structural Geology and Tectonic Evolution of the Algarve Basin, South Portugal. Ph.D. thesis, Imperial College, University of London

Tucholke BE, Sawyer DS, Sibuet J-C (2007) Break-up of the Newfoundland-Iberia rift. Imaging, mapping and modelling continental lithisohere extension and breakup. In: Karner GD, Manatschal G, Pinheiro LM (eds) Imaging, mapping and modelling continental lithosphere extension and breakup. Geological Society, London, Special Publications, vol 282, pp 9–46. https://doi.org/10.1144/SP282.2

Verati C, Rapaille C, Féraud G, Marzoli A, Bertrand H, Youbi N (2007) 40Ar/39Ar ages and duration of the Central Atlantic Magmatic Province volcanism in Morocco and Portugal and its relation to

the Triassic–Jurassic boundary. Palaeogeogr Palaeoclimatol Palaeoecol 244:308–325

Wilson RCL, Hiscott RN, Willis MG, Gradstein FM (1989) The Lusitanian Basin of West-central Portugal: Mesozoic and Tertiary tectonic, stratigraphic and subsidence history. In: Tankard AJ, Balkwill H (eds) Extensional tectonics and stratigraphy of the North Atlantic margins, vol 46. AAPG Memoir, Tulsa, pp 341–361